

# The Matsuno–Gill model on the sphere

Ofer Shamir<sup>1</sup>, Chaim I. Garfinkel<sup>2</sup>, Edwin P. Gerber<sup>1</sup> and Nathan Paldor<sup>2,†</sup>

<sup>1</sup>Courant Institute of Mathematical Sciences, New York University, New York, NY 10012, USA

<sup>2</sup>Fredy and Nadine Herrmann Institute of Earth Sciences, Hebrew University of Jerusalem, Edmond J. Safra Campus, Givat Ram, Jerusalem 91904, Israel

(Received 23 December 2022; revised 22 March 2023; accepted 23 April 2023)

We extend the Matsuno–Gill model, originally developed on the equatorial  $\beta$ -plane, to the surface of the sphere. While on the  $\beta$ -plane the non-dimensional model contains a single parameter, the damping rate  $\gamma$ , on a sphere the model contains a second parameter, the rotation rate  $\epsilon^{1/2}$  (Lamb number). By considering the different combinations of damping and rotation, we are able to characterize the solutions over the  $(\gamma, \epsilon^{1/2})$  plane. We find that the  $\beta$ -plane approximation is accurate only for fast rotation rates, where gravity waves traverse a fraction of the sphere's diameter in one rotation period. The particular solutions studied by Matsuno and Gill are accurate only for fast rotation and moderate damping rates, where the relaxation time is comparable to the time on which gravity waves traverse the sphere's diameter. Other regions of the parameter space can be described by different approximations, including radiative relaxation, geostrophic, weak temperature gradient and non-rotating approximations. The effect of the additional parameter introduced by the sphere is to alter the eigenmodes of the free system. Thus, unlike the solutions obtained by Matsuno and Gill, where the long-term response to a symmetric forcing consists solely of Kelvin and Rossby waves, the response on the sphere includes other waves as well, depending on the combination of  $\gamma$  and  $\epsilon^{1/2}$ . The particular solutions studied by Matsuno and Gill apply to Earth's oceans, while the more general  $\beta$ -plane solutions are only somewhat relevant to Earth's troposphere. In Earth's stratosphere, Venus and Titan, only the spherical solutions apply.

**Key words:** rotating flows, atmospheric flows, shallow water flows

## 1. Introduction

One of the pillars of tropical meteorology is the Matsuno–Gill model, which provides a simple, yet informative, description of the circulation patterns in the tropics using

† Email address for correspondence: [nathan.paldor@mail.huji.ac.il](mailto:nathan.paldor@mail.huji.ac.il)

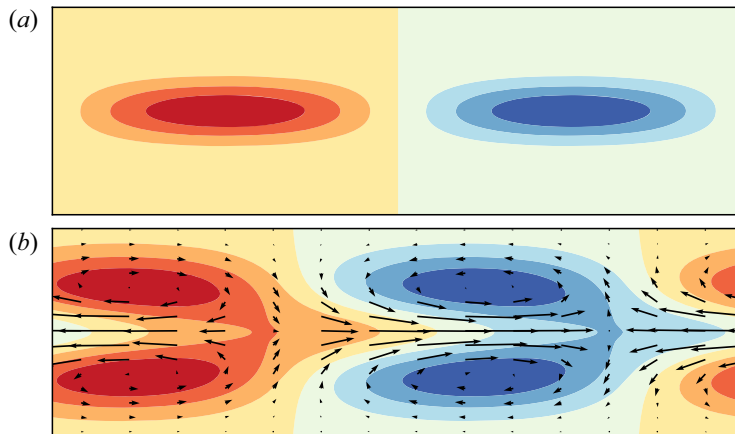


Figure 1. The fleur-de-lis on the  $\beta$ -plane: rendition of figure 9 in Matsuno (1966). (a) The mass source/sink – forcing. (b) The steady-state geopotential (colour shading) and winds (arrows) – response. The meridional domain extends from  $-18^\circ$  to  $18^\circ$ . The equatorial Rossby deformation radius is  $5.7^\circ$  (637 km). Contours range from  $-1$  (deep blue) to  $1$  (strong red) every  $0.25$ .

the framework of the forced-dissipated rotating shallow-water equations (RSWEs). The model is named after the seminal works of Matsuno (1966) and Gill (1980) who studied these equations on the infinite equatorial  $\beta$ -plane and obtained steady-state solutions in response to heating that is meridionally variable (i.e. the Hadley circulation) and zonally asymmetric (i.e. the Walker circulation) subject to linear damping (i.e. Rayleigh friction) and thermal relaxation (i.e. Newtonian cooling).

While studying ‘quasi-geostrophic’ motions in the equatorial area, Matsuno obtained explicit expressions for the frequencies and latitude-dependent amplitudes of zonally propagating wave solutions of the (free) RSWEs on the infinite equatorial  $\beta$ -plane by solving for the eigenvalues and corresponding eigenfunctions of the associated eigenvalue problem (Matsuno 1966). Using those eigensolutions, Matsuno then obtained the spatial distribution of forced stationary waves for general forms of forcing (provided that they can be spanned by the eigenfunctions) and examined the particular response to a (stationary) ‘Kelvin wave’ mass source/sink (the first eigensolution of the free RSWEs). For small dissipation rates, the resulting surface elevation consists of equatorially symmetric ridges and troughs that straddle the equator, and were described by Matsuno as the ‘petals’ of a flower (figure 9 in Matsuno (1966), rendition in figure 1 of the present work). Inspired by Matsuno’s imagery, and considering the prevalence of this pattern in tropical meteorology, we refer to it as the ‘fleur-de-lis’ after the iconic emblem (see § 7 of the supplementary material available at <https://doi.org/10.1017/jfm.2023.369>). By this, we mean to emphasize the essential features of the Matsuno–Gill pattern: an eastward tongue on the equator (the stem) and two off-equatorial ‘petals’ extending westward, symmetric across the equator. Physically, the resulting flow pattern can be explained in terms of geostrophic adjustment to a mass source introduced into a quiescent state.

Likewise, while studying the heat-induced tropical circulation, Gill used the forced-dissipated RSWEs on the infinite equatorial  $\beta$ -plane (under the long-wave approximation) to study the stationary circulation patterns in response to a zonally localized heat source (with respect to an infinite zonal domain) with a geopotential forcing corresponding to Kelvin and mixed Rossby gravity (MRG) waves (the first and second eigensolutions of the free RSWEs, respectively; Gill 1980). A key feature of

Gill's analysis is the description of the steady circulation in terms of the constituent waves. For small dissipation rates, the response to symmetric heating about the equator consists of a westward-propagating Rossby wave and an eastward-propagating Kelvin wave. The former manifests as off-equatorial pressure cells corresponding to the petals of the fleur-de-lis, while the latter manifests as an elongated equatorial pressure cell corresponding to the stem. The response to antisymmetric heating about the equator consists of a westward-propagating MRG wave and an eastward-propagating inertia gravity (IG) wave. The combination of the two is manifested by an off-equatorial pressure dipole centred to the west of the forcing and elongated westwards. Gill then studied more general forcings as a combination of these former two cases.

Since its formulation, the Matsuno–Gill model has proven useful for understanding most major tropical phenomena. In the context of the Madden–Julian oscillation, the same analysis used by Gill for finding the steady-state responses was used to find the transient response to an easterly moving heat source mimicking a moving convective region, but for a frame of reference that travels with the heat source (Chao 1987; Biello & Majda 2005; Majda & Stechmann 2009; Sobel & Maloney 2012; Adames & Kim 2016; Kacimi & Khouider 2018). In the context of the Intertropical Convergence Zone (ITCZ), the Matsuno–Gill model with a Bjerknes feedback was used to study the double ITCZ (Adam 2018), and the model was also used to study the effects of the eastern Pacific El Niño and central Pacific El Niño on the ITCZ (Zhu *et al.* 2018). In the context of equatorial super-rotation, it was shown that the Matsuno–Gill model does not exhibit equatorial super-rotation due to an inconsistent parametrization of vertical momentum transfer in the model (Showman & Polvani 2010). The model was also used to interpret momentum flux patterns in the transition to strong equatorial super-rotation (Arnold, Tziperman & Farrell 2012). Lutsko (2018) studied the response to diabatic heating in an idealized, dry general circulation model, and found that equatorial super-rotation is associated with the breakdown of the linear regime where the Matsuno–Gill solutions apply. The Matsuno–Gill model was also used as a prototype model for studying the weak temperature gradient approximation, where it was shown that under this approximation, the Rossby wave part of the response is not trapped equatorially, and the model has a far-field response to a localized tropical heating (Bretherton & Sobel 2003). Finally, the Matsuno–Gill model has been applied recently in the study of stratospheric chemistry (Wilka *et al.* 2021).

Physically, for the Matsuno–Gill model to be relevant, the temporal variations of the forcing need to be slow compared to the relaxation time of the atmosphere, such that the steady-state solutions are applicable. In addition, the meridional extent of the forcing needs to be sufficiently small so that the response may be described using the  $\beta$ -plane approximation. In Matsuno's words (paraphrasing to remove equation numbers and nomenclature):

It may be plausible to assume that external forces or inhomogeneous terms are not zero only in the finite distance from the equator.

(Matsuno 1966)

However, one can think of long-term forcing on Earth with global-scale meridional extents. For example, atmospheric stationary waves forced by asymmetries in the lower boundary, such as topography, ocean heat fluxes and land–sea contrast. Certainly, the meridional extent of all three forcings is global, and their temporal variations are slow compared to the relaxation time of the atmosphere. One can also consider the response to long-term radiative forcing at the top of the atmosphere. For example, the annually

averaged net radiative forcing varies in the meridional direction as a cosine of the latitude from approximately  $+75 \text{ W m}^{-2}$  (heating) at the equator to  $-100 \text{ W m}^{-2}$  (cooling) at the poles. A final example is the steady-state response to aerosol-induced stratospheric heating (surface cooling) following volcanic eruptions. The typical lifespan of aerosols in the stratosphere is approximately a year, which is long compared to the relaxation time of their induced radiative forcing, and their spatial coverage in some major events can be substantial. For example, the meridional extent of the aerosol-induced heating following the 1991 Mount Pinatubo eruption extended from approximately  $-45^\circ\text{S}$  to  $45^\circ\text{N}$  (Toohey *et al.* 2014; DallaSanta, Gerber & Toohey 2019). The global dynamical response to these external forcings cannot be described fully by a theory limited to the equatorial  $\beta$ -plane.

Mathematically, the analyses by Matsuno (1966) and Gill (1980) were greatly simplified by the fact that the free non-dimensional RSWEs on the infinite equatorial  $\beta$ -plane can be made parameter-free. In contrast, the free RSWEs on the sphere can be reduced to only a single non-dimensional parameter, referred to as the Lamb number and denoted here by  $\epsilon = (2\Omega a)^2/gH$  (where  $a$ ,  $g$  and  $\Omega$  denote the mean radius, gravitational acceleration and angular frequency of the celestial body in question, and  $H$  denotes the mean layer thickness of the layer of fluid in question). In addition, the analyses by Matsuno (1966) and Gill (1980) were also simplified by the availability of exact analytic solutions for the free RSWEs on the infinite equatorial  $\beta$ -plane. However, on the sphere, there are only approximate solutions for small and large  $\epsilon$ . Specifically, as discussed in Garfinkel *et al.* (2017), the free RSWEs on the infinite equatorial  $\beta$ -plane approximate the free RSWEs on the sphere in the limit  $\epsilon \rightarrow \infty$ , but only to zero order in  $\epsilon^{-1/4}$ . More accurate approximations in this limit were obtained by De-Leon & Paldor (2011). Like the infinite equatorial  $\beta$ -plane, the meridional part of the solutions obtained by De-Leon & Paldor (2011) corresponds to the Hermite functions, but of a scaled latitude. (Similar results were obtained by Longuet-Higgins (1968), albeit only for zonal wavenumbers of order 1.) In the opposite limit, as  $\epsilon \rightarrow 0$ , the free RSWEs on the sphere can be approximated to zero order in  $\epsilon^{1/2}$  by the non-rotating shallow-water equations, where the meridional part of the solutions is described by the associated Legendre polynomials. Higher-order approximations were obtained by Hough (1897, 1898) and Longuet-Higgins (1968). In fact, the problem of forced oscillations of infinitely long period (i.e. stationary solutions) in the RSWEs on the sphere is also studied in Hough (1897), but without dissipation. In addition, Paldor, De-Leon & Shamir (2013) obtained a simpler expression using Gegenbauer functions to approximate the meridional part of the solutions in this limit.

The value of the Lamb number on Earth varies by four orders of magnitude from  $\epsilon = 10$ , corresponding to gravity wave speed  $300 \text{ m s}^{-1}$  associated with the barotropic mode in the atmosphere (Fritts & Alexander 2003), to  $\epsilon = 10^5$ , corresponding to gravity wave speed  $3 \text{ m s}^{-1}$  associated with the first baroclinic mode in the oceans (Chelton *et al.* 1998). Hence it is not clear whether the asymptotic solutions (either  $\epsilon \rightarrow 0$  or  $\epsilon \rightarrow \infty$ ) from these earlier works are relevant for the response to a Matsuno–Gill-like forcing on the sphere. In addition, Gill studied the response to a dissipation rate, denoted here by  $\gamma$ , corresponding to a relaxation time of approximately two days. However, the typical relaxation time of the atmosphere varies by at least one order of magnitude, from  $O(1)$  to  $O(10)$  days, and is difficult to constrain by observations. Finally, on celestial bodies that rotate more slowly than Earth, for example, Venus and Titan, erstwhile equatorial wave modes are observed to extend well into mid-latitudes (Svedhem *et al.* 2007; Mitchell *et al.* 2011; Yamamoto 2019; Peralta *et al.* 2020), limiting the relevance the  $\beta$ -plane solutions.

The ubiquity of the Matsuno–Gill model in the study of the tropics, the existence of large-scale, long-term, forcing on Earth, and the dependence of the  $\beta$ -plane approximation on the Lamb number, all motivate study of the Matsuno–Gill model on the sphere. Specifically, a key feature of the present work is the analysis of the Matsuno–Gill model on the sphere in the  $(\gamma, \epsilon^{1/2})$  plane.

The paper is organized as follows. In § 2, we introduce the governing equations, and provide some general considerations employed in the subsequent sections. In § 3, we describe the suitable choice of the applied forcing in order to extend the original works of Matsuno and Gill. In § 4, we describe numerically obtained solutions of the Matsuno–Gill model on the sphere in representative cases. In § 5, we describe some ‘simple solutions of the heat induced circulation’ (paraphrasing Gill), and discuss their applicability to Earth, Venus and Titan in § 6. In § 7, we examine the wave composition of the response in the Matsuno–Gill model on the sphere. In § 8, we examine the response to a localized forcing (both zonally and meridionally) akin to that used by Gill. Finally, the results are summarized and discussed in § 9.

## 2. Governing equations and preliminary considerations

The Matsuno–Gill model describes steady-state wave solutions of the forced-dissipated RSWEs. In their original works, Matsuno (1966) and Gill (1980) obtained exact analytic solutions of the linearized version of these equations on the infinite equatorial  $\beta$ -plane for particular forms of forcing and dissipation terms. We extend the Matsuno–Gill model to the surface of the sphere, using the same forms of forcing and dissipation. In particular, following Matsuno and Gill, we assume the following.

- (i) There is no momentum forcing, only a prescribed ‘heat/mass’ source added to the continuity equation. The extension of the forcing used by Matsuno and Gill to the sphere is described in more detail in § 3.
- (ii) We let the dissipative terms in the momentum equations and the continuity equation take the forms of Rayleigh friction and Newtonian cooling, respectively, and assume that they can all be characterized by the same time scale. While such forms of dissipation are likely not the most suitable ones for any particular application, as noted by Gill (1980), they are the simplest.

Let  $a$ ,  $g$  and  $\Omega$  denote the mean radius, gravitational acceleration and angular frequency of the celestial body in question, and let  $H$  denote the mean thickness of the layer of fluid in question. Then, using  $a$  as the horizontal length scale, and  $\sqrt{a^2/gH}$  as the time scale (which implies that  $\sqrt{gH}$  is the horizontal velocity scale), the linearized forced-dissipated (time-dependent) RSWEs in spherical coordinates can be written in non-dimensional form as

$$\frac{\partial u}{\partial t} - \epsilon^{1/2} v \sin \phi + \frac{1}{\cos \phi} \frac{\partial \Phi}{\partial \lambda} = -\gamma u, \tag{2.1a}$$

$$\frac{\partial v}{\partial t} + \epsilon^{1/2} u \sin \phi + \frac{\partial \Phi}{\partial \phi} = -\gamma v, \tag{2.1b}$$

$$\frac{\partial \Phi}{\partial t} + \frac{1}{\cos \phi} \left[ \frac{\partial u}{\partial \lambda} + \frac{\partial}{\partial \phi} (v \cos \phi) \right] = -\gamma \Phi + Q, \tag{2.1c}$$

where  $t$  denotes time,  $0 \leq \lambda < 2\pi$  and  $-\pi/2 \leq \phi \leq \pi/2$  denote the longitudinal and latitudinal angles,  $u$  and  $v$  denote the zonal and meridional velocity components,

$\Phi$  denotes the geopotential height anomaly (where the non-dimensional mean geopotential equals 1),  $\gamma > 0$  denotes the damping/cooling coefficient,  $Q = Q(\lambda, \phi)$  is a prescribed forcing (meaning that  $Q$  is a known function of the longitude and latitude), and  $\epsilon$  is the Lamb number, defined by

$$\epsilon = (2\Omega a)^2/gH. \tag{2.2}$$

Based solely on the different ways of grouping its constituent parameters, the Lamb number can be interpreted in a number of ways. Depending on the appropriate length and time scale in a particular application,  $\epsilon^{1/2}$  may play the role of the (inverse) Rossby number or the Froude number. Instead, the Lamb number is more consistently interpreted based on its location in the equations, and not based on its constituent parameters. Thus, under the preset scaling, where  $\epsilon^{1/2}$  appears in front of the Coriolis terms in the momentum equations, it plays the role of the non-dimensional rate of rotation (measured relative to the time over which a gravity wave can appreciably propagate around the sphere).

The validity of the linearization depends on both the amplitude and the spatial variability of the forcing. For highly oscillating  $Q$ , the resulting  $u, v, \Phi$  fields can also be highly oscillating, and the advection terms can be non-negligible even for small forcing amplitude. In the present work, we take the term ‘the Matsuno–Gill model’ to mean the linearized equations, so only low Fourier modes should be considered. In practice, the forcing can often be treated as slowly varying, e.g. for the purpose of providing simple descriptions of the Hadley and Walker circulations. Yet the validity of the linearization should be confirmed on a per-case basis, and the problem of nonlinear adjustment of the forced-dissipated RSWEs merits additional study.

The stationary system is obtained by setting  $\partial/\partial t$  equal to zero in system (2.1a–c), yielding

$$-\epsilon^{1/2}v \sin \phi + \frac{1}{\cos \phi} \frac{\partial \Phi}{\partial \lambda} = -\gamma u, \tag{2.3a}$$

$$\epsilon^{1/2}u \sin \phi + \frac{\partial \Phi}{\partial \phi} = -\gamma v, \tag{2.3b}$$

$$\frac{1}{\cos \phi} \left[ \frac{\partial u}{\partial \lambda} + \frac{\partial}{\partial \phi}(v \cos \phi) \right] = -\gamma \Phi + Q, \tag{2.3c}$$

which we shall refer to as the Matsuno–Gill model on the sphere. Aside from some trivial changes associated with the choice of scaling and the spherical geometry, this is precisely the fundamental system studied in the planar versions of the model, i.e. system (30) of Matsuno (1966), and equations (2.6)–(2.8) of Gill (1980). Note, however, that Gill subsequently imposed the long-wave approximation, which is tantamount to neglecting  $-\gamma v$  on the right-hand side of (2.3b). The way in which this spherical model degenerates to the planar Matsuno–Gill problem when  $\epsilon \rightarrow \infty$  is examined in § 5.1.

Before continuing, we introduce one further simplification. Observe that the coefficients of the Matsuno–Gill model (2.3a–c) are  $\lambda$ -independent. Thus we may replace each  $\lambda$ -dependent quantity with a Fourier series in  $\lambda$ , and consider each Fourier mode separately. Specifically, we assume that the forcing  $Q$  and the unknowns  $u, v, \Phi$  all have the form

$$\zeta(\lambda, \phi) = \sum_{m=-\infty}^{\infty} \zeta^m(\phi) \exp(im\lambda), \tag{2.4}$$



where  $\zeta$  is any of the  $\{u, v, \Phi, Q\}$  variables, and  $\zeta^m(\phi)$  is the corresponding latitude-dependent coefficient. The resulting system for each individual Fourier mode  $m$  is then

$$-\epsilon^{1/2}v^m \sin \phi + \frac{im}{\cos \phi} \Phi^m = -\gamma u^m, \tag{2.5a}$$

$$\epsilon^{1/2}u^m \sin \phi + \frac{d\Phi^m}{d\phi} = -\gamma v^m, \tag{2.5b}$$

$$\frac{1}{\cos \phi} \left[ imu^m + \frac{d}{d\phi}(v^m \cos \phi) \right] = -\gamma \Phi^m + Q^m. \tag{2.5c}$$

Similarly, Matsuno assumed a zonally periodic forcing and studied the latitude-dependent boundary value problem remaining after a Fourier decomposition in the zonal direction. In contrast, Gill assumed a zonally localized (aperiodic) forcing and studied the longitude-dependent problem remaining after expanding the latitudinal part in terms of the eigensolutions of the free problem. In § 8, we show how the solutions of (2.5a–c) combine to yield the response to a localized forcing akin to the one used by Gill.

A key property of the free RSWEs on the sphere is the existence of two qualitatively different solution regimes: an equatorial regime, in which the solutions are non-negligible only in the vicinity of the equator (i.e. equatorially trapped solutions), and a global regime, in which the solutions are non-negligible at all latitudes. Generally speaking, the former is realized in the limit of large Lamb number, while the latter is realized in the limit of small Lamb number. More accurately, as noted in Boyd (1985, 2018) and Boyd & Zhou (2008), for a given Lamb number, the equatorial regime is also realized in the limit of large zonal wavenumber. However, as discussed above, the linearization may no longer be applicable if the solutions have appreciable power at high Fourier modes.

Finally, the free problem consists of finding the dispersion relations and latitude-dependent amplitudes of zonally propagating waves, i.e. solutions of the form

$$\{u(t, \lambda, \phi), v(t, \lambda, \phi), \Phi(t, \lambda, \phi)\} = \{u^m(\phi), v^m(\phi), \Phi^m(\phi)\} \exp [i(m\lambda - \omega t)], \tag{2.6}$$

where  $\omega$  is the wave frequency. Setting  $\gamma = 0$  and  $Q = 0$  in (2.1a–c) and substituting (2.6) yields the following eigenvalue problem for each Fourier mode  $m$  of the free waves:

$$\mathbf{L}X = i\omega X, \tag{2.7}$$

where

$$\mathbf{L} = \begin{bmatrix} 0 & -\epsilon^{1/2} \sin \phi & \frac{im}{\cos \phi} \\ \epsilon^{1/2} \sin \phi & 0 & \frac{d}{d\phi} \\ \frac{im}{\cos \phi} & \left( \frac{d}{d\phi} - \tan \phi \right) & 0 \end{bmatrix}, \quad X = \begin{bmatrix} u^m \\ v^m \\ \Phi^m \end{bmatrix}. \tag{2.8a,b}$$

Formally, the above equation is equivalent to the Matsuno–Gill model (2.5a–c) with  $\omega = i\gamma$  (and  $Q = 0$ ). However, the two problems are different in essence. The free problem consists of an eigenvalue problem for the unknown eigenvalue(s)  $\omega$ , while the dissipated problem consists of a boundary value problem for given (i.e. known) values of  $\gamma$ .

### 3. The prescribed forcing

Before comparing solutions of the Matsuno–Gill model on the equatorial  $\beta$ -plane with those on the sphere, we first ensure that the two converge in the appropriate limit. As was shown in Garfinkel *et al.* (2017), for any fixed zonal wavenumber, free RSWEs on the equatorial  $\beta$ -plane approximate free RSWEs on the sphere in the limit  $\epsilon \rightarrow \infty$ . Consider the relation  $\omega = i\gamma$  between the frequency  $\omega$  in solutions of the free system and the dissipation  $\gamma$  in the steady-state system. For the two systems to converge, the prescribed forcings must also be identical, which guides the following choices.

Starting with the latitudinal dependence, the forcing used by Matsuno and Gill (the latter only in response to a symmetric forcing) in the continuity equation corresponds to the geopotential height field of a Kelvin wave on the equatorial  $\beta$ -plane. Hence a natural extension of the forcing is the geopotential height field corresponding to the ‘Kelvin’ wave on the sphere. The existence of a (nearly) non-dispersive wave that converges to the equatorial Kelvin wave on the  $\beta$ -plane for  $\epsilon \rightarrow \infty$  was verified in Garfinkel *et al.* (2017). From the point of view of the eigenvalue problem associated with the free RSWEs on the sphere, however, this wave is more accurately classified as the lowest mode eastward IG wave. Likewise, the forcing used by Gill in the continuity equation in response to a meridionally antisymmetric heating corresponds to the geopotential height field of an equatorial MRG wave. Hence a natural extension to the present work is the geopotential height field corresponding to the MRG wave on the sphere, whose existence was verified in Paldor *et al.* (2018).

Next, with regard to the longitudinal dependence, as discussed in § 2, we may consider each Fourier mode separately. Hence, without loss of generality, we assume that the forcing consists of a single Fourier mode, and study the response to the representative case  $m = 5$ . This value is chosen specifically in order to reproduce Matsuno’s solutions for large values of  $\epsilon$  (fast rotation). Specifically, the results presented in figure 9 of Matsuno (1966) (figure 1 of the present work) were obtained using a planar (non-dimensional) wavenumber  $k = 0.5$ . The spherical wavenumber of the present work is related to the latter by  $m = \epsilon^{1/4}k$ . Hence  $k = 0.5$  corresponds to  $m = 5$  for  $\epsilon = 10^4$ , which is used throughout this work as a representative value of large  $\epsilon$ . Due to the periodicity of the spherical coordinate system,  $m$  takes only integer values, hence particular values of  $k$  correspond to acceptable values of  $m$  only for certain values of  $\epsilon$ . The response to a wavenumber 1 forcing is qualitatively different from all other wavenumbers  $m > 1$  in that the regular solutions of (2.5a–c) have non-vanishing velocities at the poles, and is left for the supplementary material. The case  $m = 0$  requires special treatment and is of lesser interest in the context of the Matsuno–Gill model, which is concerned with zonally asymmetric forcing.

### 4. Representative solutions

In the absence of exact analytic solutions for the Matsuno–Gill model on the sphere for arbitrary values of  $\gamma$  and  $\epsilon^{1/2}$ , numerical approximations can be obtained readily. In the present work, we use a Chebyshev collocation method (e.g. Trefethen 2000) to solve (2.5a–c) as follows. For each wavenumber  $m$ , we first solve the eigenvalue problem associated with zonally propagating wave solutions of the free RSWEs to obtain the latitude-dependent amplitudes of the Kelvin and MRG waves. For any value of  $\epsilon^{1/2}$ , the Kelvin wave can be identified as the first wave with  $\omega > m$  (assuming  $m > 0$  by convention; Garfinkel *et al.* 2017). In contrast, the identification of the MRG wave depends on the value of  $\epsilon^{1/2}$ . The point where the MRG transitions from an IG wave at small



	Light damping	Moderate damping	Heavy damping
Fast rotation	LF ( $10^{-2}$ , $10^2$ )	MF (1, $10^2$ )	HF ( $10^2$ , $10^2$ )
Moderate rotation	LM ( $10^{-2}$ , 1)	MM (1, 1)	HM ( $10^2$ , 1)
Slow rotation	LS ( $10^{-2}$ , $10^{-2}$ )	MS (1, $10^{-2}$ )	HS ( $10^2$ , $10^{-2}$ )

Table 1. Particular values of the  $(\gamma, \epsilon^{1/2})$  plane used throughout the study. For the sake of brevity, we denote the different combinations using a two-letter acronym, where the first letter corresponds to one of the three rates of damping, and the second letter corresponds to one of the three rates of rotation, e.g. LF denotes the case of light damping and fast rotation.

wavenumbers to a Rossby wave at large wavenumbers is  $m^* = \epsilon^{1/4}/\sqrt{2}$  (Paldor *et al.* 2018). For  $m < m^*$ , the MRG is identified as the first wave with  $-\omega > m$ , while for  $m > m^*$ , it is identified as the first wave with  $-\omega < m$  (assuming  $m > 0$  by convention). Having solved for the Kelvin and MRG waves, we then substitute the resulting geopotential height for  $Q^m$  and solve the boundary value problem associated with the Matsuno–Gill model (2.5a–c). For the sake of simplicity, we normalize the prescribed forcing by its global absolute maximum, i.e.  $\max_{\phi} |Q^m|$ . In general, this choice could be inconsistent with the linearization, but it has no implications in the present work, where the system of equations is linearized from the outset.

We provide an overview of the numeric approximations in representative cases. As detailed in §3, we choose wavenumber  $m = 5$  as a representative wavenumber, which corresponds to the value used by Matsuno for the planar wavenumber  $k = 0.5$  at  $\epsilon^{1/4} = 10$ . The results were verified qualitatively for wavenumbers 2, 8 and 1 (see figures 1–6 in the supplementary material). The case  $m = 1$  is qualitatively different from all other wavenumbers  $m > 1$  in that the regular solutions of (2.5a–c) have non-vanishing velocities at the poles (see §§2 and 3 in the supplementary material).

To sample the  $(\gamma, \epsilon^{1/2})$  plane, we examine the nine combinations of light/moderate/heavy damping and slow/moderate/fast rotation. The particular values of  $\gamma$  and  $\epsilon^{1/2}$  used throughout this study to represent these regimes are summarized in table 1. Recall that our time scale is  $\sqrt{a^2/gH}$ . Thus under the present scaling, the damping and rotation rates are measured relative to the time taken for a gravity wave with speed  $\sqrt{gH}$  to propagate distance  $a$ . For example, ‘fast rotation’ implies that the celestial body revolves around itself well before a gravity wave can travel a radial distance. Similarly, ‘light damping’ implies that a gravity wave will propagate around the sphere before being appreciably damped. This differs from Matsuno’s scaling, where time is scaled on the equatorial Rossby deformation time, and ‘light’ damping implies that a gravity wave will propagate ‘far enough’ to feel the effects of rotation before being appreciably damped.

As detailed in §5.1, the conversion between the damping in Matsuno’s scaling (denoted here by  $\alpha$ ) and the present scaling is  $\alpha = \epsilon^{-1/4}\gamma$ . Thus for  $\epsilon^{1/4} = 10$  (where the equatorial  $\beta$ -plane is found to be accurate),  $\gamma = 10^{-2}$  (our light damping) corresponds to  $\alpha = 10^{-3}$ , and  $\gamma = 10^2$  (our heavy damping) corresponds to  $\alpha = 10^1$ . Equivalently, for the same value of  $\epsilon$ , Matsuno’s damping rate  $\alpha = 0.2$  corresponds to  $\gamma = 2$ , i.e. moderate damping in the present scaling.

Figures 2 and 3 provide representative solutions of the Matsuno–Gill model on the sphere in response to a (symmetric) Kelvin and an (antisymmetric) MRG wave-5 forcing, respectively. The columns show different variables, the rows different combinations of  $\gamma$  and  $\epsilon^{1/2}$ . The meridional domain in each of these figures extends from the south pole to the north pole. For optimal presentation, the longitudinal domain corresponds to one zonal period ( $2\pi/5$ ). In addition, each panel is normalized on its global absolute maximum, indicated within the white text box at the bottom of each panel.

Our first observation from the representative solutions in figures 2 and 3 is that both equatorial and global solution regimes are found across the  $(\gamma, \epsilon^{1/2})$  plane. The solutions transition from equatorial at fast rotation rates to global at moderate or slow rotation rates, regardless of the damping rate. Accordingly, for the Matsuno–Gill model on the equatorial  $\beta$ -plane to approximate solutions on the sphere, the celestial body in question must be rotating rapidly. Indeed, looking at the response to a Kelvin wave-5 forcing in figure 2, we identify the fleur-de-lis in the geopotential height field in figure 2(b)(ii) with moderate damping (red square). Figure 4 zooms in on the prescribed forcing (figure 4a) and geopotential height (figure 4b) obtained numerically (shadings), compared to the analytic solutions obtained by Matsuno (contours): our forcing yields solutions that converge to Matsuno’s, confirming it as a natural extension of the latter. Likewise, figure 5 zooms in on the zonal (figure 5a) and meridional (figure 5b) winds obtained numerically (shadings), compared to Matsuno’s solutions (contours). Clearly, the fleur-de-lis on the sphere converges to the fleur-de-lis on the  $\beta$ -plane, but only when the gravity wave propagation time scale is small relative to rotation and comparable to the damping. In all other cases, we obtain substantially different solution patterns.

Our second key take-away from the representative solutions concerns the balance of the forcing. For light damping (regardless of rotation rate), the divergence is identical to the applied forcing. From (2.5a–c), for light damping, the dissipation term is negligible compared to the forcing in the continuity equation, leaving only the divergence to balance the forcing. As the damping increases, the divergence remains spatially similar to the forcing (except for moderate-to-heavy damping and fast rotation), but it is orders of magnitude smaller. From (2.5a–c), with heavy damping, the forcing in the continuity equation is now balanced by the dissipation term. This is confirmed in figures 2(c,f,i) and 3(c,f,i) (our heavy damping rate is  $\gamma = 10^2$ ; table 1). Note that the weak divergence with heavy damping follows from the low amplitudes of the winds. While negligible, it is never identically zero. This is in contrast to purely two-dimensional flows, where the zonal divergence and meridional divergence compensate each other, so the total divergence is identically zero.

Our third observation from the representative solutions is the emergence of a geostrophic balance between the geopotential height field and the zonal and meridional wind fields at light damping and fast-to-moderate rotation rates (figures 2a,d and 3a,d). From (2.5a–c), the dissipation term becomes negligible for light damping, leaving the Coriolis and pressure gradient terms to balance. Global-scale geostrophic balance is attainable by maintaining a vanishing geopotential height gradient at the equator (for  $m > 0$  this implies that  $\Phi = 0$  along the equator). For slow rotation rates, the Coriolis term is also small, and the dissipation term cannot be neglected, explaining the lack of geostrophic balance. To a lesser extent (only outside the equator), the response at moderate damping and fast rotation rate (figures 2b and 3b) is also in near geostrophic balance, consistent with Matsuno’s observation. In all other combinations of  $\gamma$  and  $\epsilon^{1/2}$ , the solutions are qualitatively far from geostrophic.

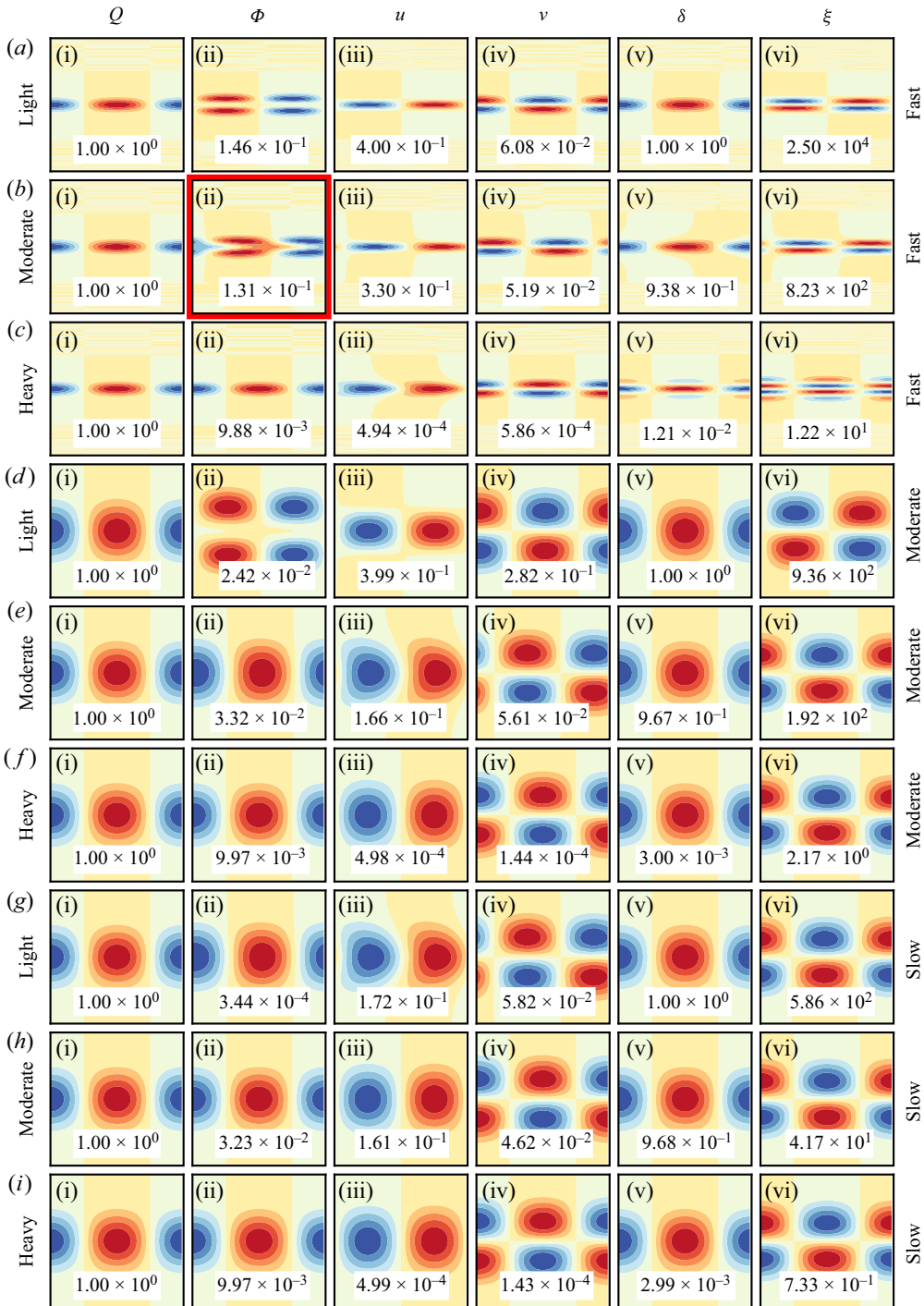


Figure 2. Steady response to a symmetric Kelvin wave-5 forcing. From (i) to (vi): the forcing, geopotential height, zonal wind, meridional wind, divergence and vorticity. Panels (a–i) correspond to the different samples of the  $(\gamma, \epsilon^{1/2})$  plane summarized in table 1. The damping and rotation rates for each case (row) are labelled on the left and right edges, respectively. The meridional domain in each panel extends from pole to pole. The longitudinal domain corresponds to one zonal period. Contours range from  $-1$  (deep blue) to  $1$  (strong red) every  $0.25$ . Each panel is normalized on its global absolute maximum, given in white text boxes. The red square around the geopotential in (b)(ii) identifies the fleur-de-lis on the sphere (figure 4b).

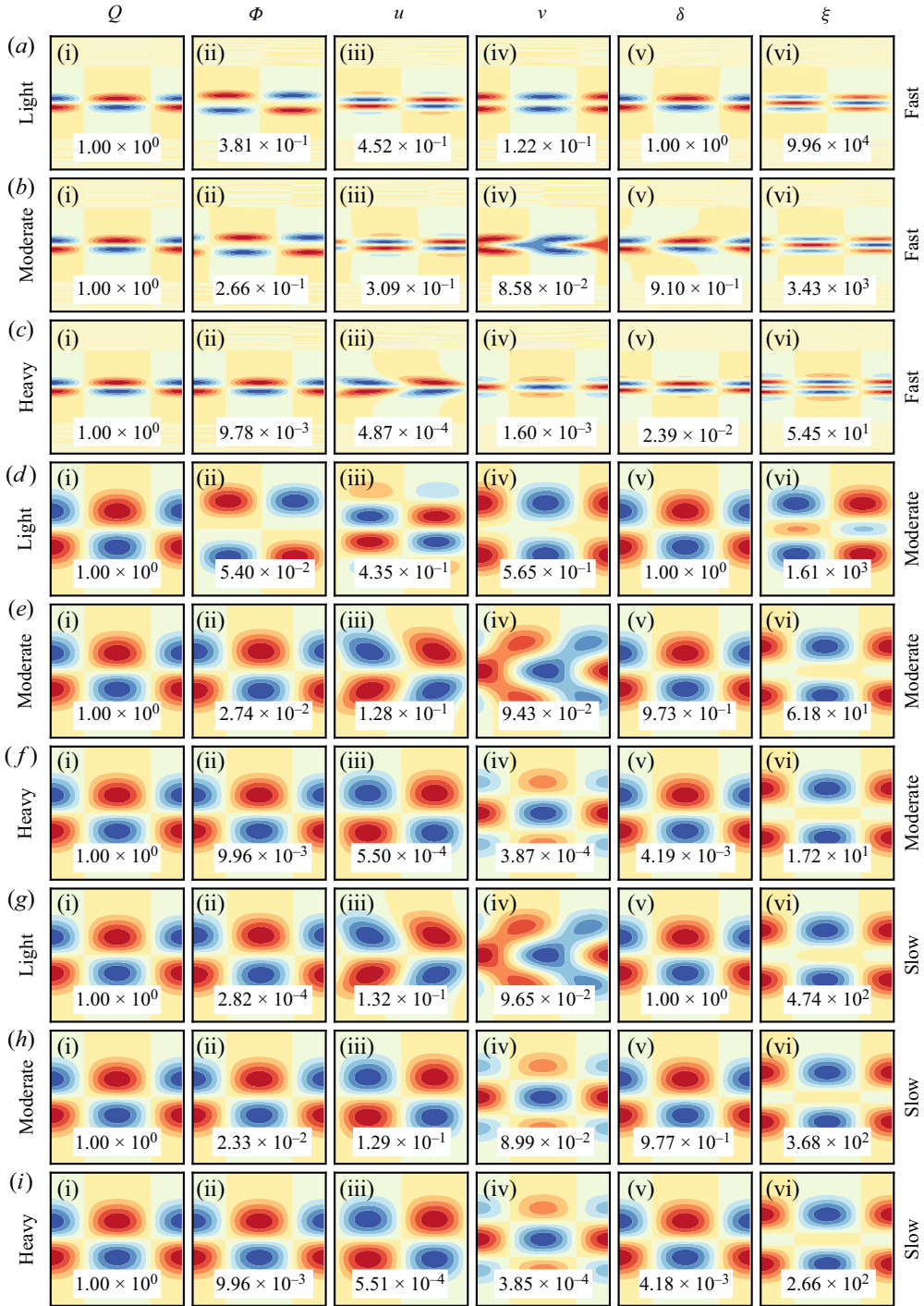


Figure 3. Steady response to a symmetric MRG wave-5 forcing. From (i) to (vi): the forcing, geopotential height, zonal wind, meridional wind, divergence and vorticity. Panels (a–i) correspond to the different samples of the  $(\gamma, \epsilon^{1/2})$  plane summarized in table 1. The damping and rotation rates for each case (row) are labelled on the left and right edges, respectively. The meridional domain in each panel extends from pole to pole. The longitudinal domain corresponds to one zonal period. Contours range from  $-1$  (deep blue) to  $1$  (strong red) every  $0.25$ . Each panel is normalized on its global absolute maximum, given in white text boxes.

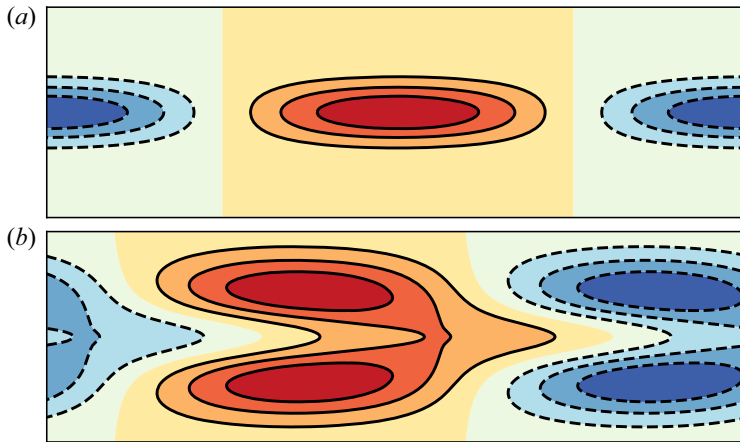


Figure 4. The fleur-de-lis on the sphere: height fields of (a) the prescribed Kelvin wave-5 forcing, and (b) the steady-state geopotential response, for moderate damping and fast rotation (figure 2b). The meridional domain extends from  $-18^\circ$  to  $18^\circ$ . Colour shading: numeric solutions obtained as detailed in § 4. Black contours: the  $\beta$ -plane approximation. Contours range from  $-1$  (deep blue) to  $1$  (strong red) every  $0.25$ .

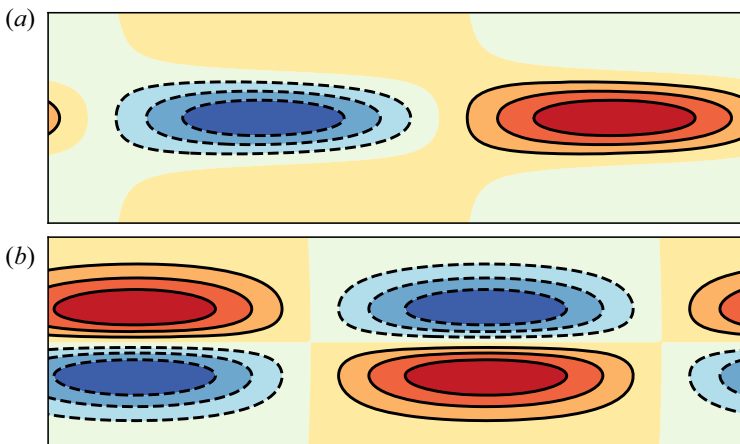


Figure 5. The steady-state (a) zonal and (b) meridional winds for moderate damping and fast rotation (figure 2b). The meridional domain extends from  $-18^\circ$  to  $18^\circ$ . Colour shading: numeric solutions obtained as detailed in § 4. Black contours: the  $\beta$ -plane approximation. Contours range from  $-1$  (deep blue) to  $1$  (strong red) every  $0.25$ .

### 5. ‘Some simple solutions for heat-induced circulation’ (paraphrasing Gill)

In the spirit of Gill (1980), we obtain approximate solutions of the ‘heat-induced’ circulation of the Matsuno–Gill model on the sphere in special cases, including the  $\beta$ -plane, radiative relaxation, geostrophic, non-rotating, weak temperature gradient and long-wave approximations. Together, the regimes covered by these approximate solutions include most of the  $(\gamma, \epsilon^{1/2})$  plane. We start with the  $\beta$ -plane approximation due to its correspondence with the original works of Matsuno and Gill. However, in terms of complexity, the simplest approximations are the radiative relaxation and geostrophic approximations, in which the unknowns  $u, v, \Phi$  can be written in terms of the prescribed forcing  $Q$  using only simple algebraic operations. The  $\beta$ -plane and non-rotating

approximations are more complex since the Matsuno–Gill model can only be reduced to a (different) boundary value problem with known solutions. The weak temperature gradient and long-wave approximations provide no tangible simplification and are included for comparison.

To quantify the validity of each approximation, we use the following ‘metric’ of relative difference:

$$\frac{\|X_r^m - X_a^m\|}{\|X_r^m\|} = \frac{\sqrt{(X_r^m - X_a^m, X_r^m - X_a^m)}}{\sqrt{(X_r^m, X_r^m)}}, \tag{5.1}$$

where  $X^m = [u^m, v^m, \Phi^m]^T$  represents the solution vector of the Matsuno–Gill model (2.5a–c), the subscript  $r$  denotes the reference solutions (the numeric solutions obtained as described in § 4), the subscript  $a$  denotes one of the approximate solutions derived below, and  $(X, \bar{X})$  denotes the inner product

$$(X, \bar{X}) = \int_{-\pi/2}^{\pi/2} X^T \bar{X} \cos \phi \, d\phi. \tag{5.2}$$

We choose the difference metric in (5.1) for two reasons. First, it assigns equal weights to all three unknowns, and hence provides an estimate of the approximation as a whole. Second, we use it for the sake of uniformity with § 7, where we will use the inner product in (5.2) to find the projections of the Matsuno–Gill model solutions on the free wave solutions of the RSWEs. We find that a value 0.1 is a convenient indicator of ‘visual’ convergence in the sense that the solutions overlap, and values lower than 0.1 lead to no visible improvements. For the sake of brevity, we refer to this metric simply as the ‘relative difference’.

### 5.1. The $\beta$ -plane approximation

As mentioned in § 2, for any fixed zonal wavenumber, the free RSWEs on the equatorial  $\beta$ -plane approximate the RSWEs on the sphere for large values of the Lamb number. We now show that this is also the case for the Matsuno–Gill model: the solutions obtained by Matsuno (1966) approximate the solutions on the sphere for sufficiently large values of  $\epsilon$ . To this end, we first re-scale system (2.3a–c) to conform with Matsuno’s scaling (Gill’s scaling differs from Matsuno’s by a factor of  $\sqrt{2}$ ), where the horizontal length scale corresponds to the equatorial Rossby deformation radius  $(\sqrt{gH}/\beta)^{1/2}$ , with  $\beta = 2\Omega/a$ , and the time scale corresponds to the Rossby deformation time  $(\sqrt{gH}\beta)^{-1/2}$ . Under Matsuno’s scaling, (2.3a–c) becomes

$$-\epsilon^{1/4} \tilde{v} \sin \phi + \frac{\epsilon^{-1/4}}{\cos \phi} \frac{\partial \tilde{\Phi}}{\partial \lambda} = -\alpha \tilde{u}, \tag{5.3a}$$

$$\epsilon^{1/4} \tilde{u} \sin \phi + \epsilon^{-1/4} \frac{\partial \tilde{\Phi}}{\partial \phi} = -\alpha \tilde{v}, \tag{5.3b}$$

$$\frac{\epsilon^{-1/4}}{\cos \phi} \left[ \frac{\partial \tilde{u}}{\partial \lambda} + \frac{\partial}{\partial \phi} (\tilde{v} \cos \phi) \right] = -\alpha \tilde{\Phi} + \tilde{Q}, \tag{5.3c}$$

where tildes are used to distinguish the quantities in Matsuno’s scaling from their counterparts in (2.3a–c), and  $\alpha$  is used to denote the damping coefficient to match



Matsuno’s notation as well. The transformation between systems (2.3a–c) and (5.3a–c) is

$$(\tilde{u}, \tilde{v}) = (u, v), \quad \tilde{\Phi} = \Phi, \quad \alpha = \epsilon^{-1/4}\gamma, \quad \tilde{Q} = \epsilon^{-1/4}Q. \quad (5.4a–d)$$

As the horizontal wind components and the geopotential remain unchanged under the above transformation, we drop the tildes above those three variables. Note that the Lamb number appears (with different powers) in front of the Coriolis term, the pressure gradient term and the divergence terms in (5.3a–c). It therefore has no unique interpretation under Matsuno’s scaling.

Next, in order to obtain the  $\beta$ -plane approximation, we must also change to local Cartesian coordinates. Using the equatorial Rossby deformation radius as the horizontal length scale, the longitude and latitude transformations are  $(\lambda, \phi) = \epsilon^{-1/4}(x, y)$ . Recall that system (2.3a–c) was simplified further by considering its Fourier decomposition in  $\lambda$ . The corresponding transformation of the zonal wavenumber is  $m = \epsilon^{1/4}k$ , where  $k$  is the planner wavenumber. Upon introducing the Fourier decomposition, system (5.3a–c) becomes

$$-\epsilon^{1/4}v^k \sin(\epsilon^{-1/4}y) + \frac{ik}{\cos(\epsilon^{-1/4}y)} \Phi^k = -\alpha u^k, \quad (5.5a)$$

$$\epsilon^{1/4}u^k \sin(\epsilon^{-1/4}y) + \frac{d\Phi^k}{dy} = -\alpha v^k, \quad (5.5b)$$

$$\frac{1}{\cos(\epsilon^{-1/4}y)} \left[ iku^k + \frac{d}{dy}(v^k \cos(\epsilon^{-1/4}y)) \right] = -\alpha \Phi^k + \tilde{Q}^k. \quad (5.5c)$$

Assuming that  $u^k, v^k, \Phi^k$  and  $\tilde{Q}^k$  can all be expanded in power series of  $\epsilon^{-1/4}$ , expanding also the trigonometric functions in Taylor series in  $\epsilon^{-1/4}y$ , and retaining only zero-order terms, yields

$$-v^k y + ik\Phi^k = -\alpha u^k, \quad (5.6a)$$

$$u^k y + \frac{d\Phi^k}{dy} = -\alpha v^k, \quad (5.6b)$$

$$iku^k + \frac{dv^k}{dy} = -\alpha \Phi^k + \tilde{Q}^k, \quad (5.6c)$$

which is identical to system (30) of Matsuno (1966) with  $F_x = F_y \equiv 0$ .

Matsuno outlines a general procedure for obtaining the solutions for arbitrary values of  $k$  and  $\alpha$  by expanding both the solution and forcing in series of the free wave solutions (the eigenfunctions of the free RSWEs on the equatorial  $\beta$ -plane). This procedure is symbolically convenient, but is less convenient when writing the analytic solutions explicitly. At least one reason is the fact that Matsuno’s expressions involve the free wave frequencies, which are given by a cubic equation. A more convenient way to derive the (exact) solutions of (5.6a–c), which was taken by Gill, is to expand the solutions and forcing in series of Hermite functions, which are the eigenfunctions of the subspace spanned by the meridional velocity. In addition, Matsuno carries out the analysis only for  $k = 0.5$  and  $\alpha = 0.2$ . Thus, for the sake of completeness, we re-derive the solutions below for arbitrary values of  $k$  and  $\alpha$ . To this end, we first rewrite system (5.6a–c) as a

single equation in  $v^k$ . Using (5.6a) to eliminate  $u^k$  from (5.6b) and (5.6c) yields

$$\frac{d}{dy} \begin{bmatrix} v^k \\ \Phi^k \end{bmatrix} = -\frac{1}{\alpha} \begin{bmatrix} iky & \alpha^2 + k^2 \\ \alpha^2 + y^2 & -iky \end{bmatrix} \begin{bmatrix} v^k \\ \Phi^k \end{bmatrix} + \begin{bmatrix} \tilde{Q}^k \\ 0 \end{bmatrix}. \quad (5.7)$$

Differentiating the first row with respect to  $y$ , and using the first and second rows to eliminate  $\Phi^k$  and  $d\Phi^k/dy$ , respectively, yields

$$\frac{d^2 v^k}{dy^2} - [\alpha^2 + k^2 + y^2 - ik\alpha^{-1}]v^k = \frac{d\tilde{Q}^k}{dy} - ik\alpha^{-1}\tilde{Q}^k. \quad (5.8)$$

Equation (5.8) can be solved by expanding both  $v^k$  and  $\tilde{Q}^k$  in series of Hermite functions, i.e.

$$v^k(y) = \sum_{n=0}^{\infty} v_n^k \Psi_n(y) = \sum_{n=0}^{\infty} v_n^k H_n(y) \exp(-\frac{1}{2}y^2), \quad (5.9)$$

where  $v_n^k$  are the expansion coefficients,  $H_n(y)$  are the (non-normalized) Hermite polynomials of degree  $n$ , and  $\Psi_n(y)$  are the Hermite functions (i.e. the Hermite polynomials multiplied by a Gaussian envelope). The latter satisfy the recurrence relations

$$x \Psi_n(x) = +\frac{1}{2} \Psi_{n+1}(x) + n \Psi_{n-1}(x), \quad (5.10a)$$

$$\frac{d\Psi_n(x)}{dx} = -\frac{1}{2} \Psi_{n+1}(x) + n \Psi_{n-1}(x), \quad (5.10b)$$

and the differential equation

$$\frac{d^2 \Psi_n(x)}{dx^2} + (2n + 1 - y^2) \Psi_n(x) = 0. \quad (5.11)$$

In general,  $\tilde{Q}^k$  is expanded similarly to  $v^k$  in (5.9). Fortunately, for large  $\epsilon$ , the geopotential height of the Kelvin and MRG waves, used here as the prescribed forcing, is proportional to a single Hermite function

$$\tilde{Q}^k(y) = Q_0 \Psi_N(y) := Q_0 H_N(y) \exp(-\frac{1}{2}y^2), \quad (5.12)$$

where  $Q_0$  is a constant amplitude, and  $N = 0, 1$  for Kelvin, MRG waves, respectively. The convergence of the wave forcing of the present work to the above expression was confirmed in figure 4(a) for a Kelvin wave-5 forcing at  $\epsilon^{1/2} = 10^2$ , and is also confirmed below for an MRG wave-5 forcing.

Substituting (5.9) and (5.12) in (5.8), and using the recurrence relations (5.10a,b) and differential equation (5.11), yields

$$\sum_{n=0}^{\infty} -[2n + 1 + \alpha^2 + k^2 - ik\alpha^{-1}]v_n^k \Psi_n = Q_0[-\frac{1}{2}(1 + ik\alpha^{-1})\Psi_{N+1} + N(1 - ik\alpha^{-1})\Psi_{N-1}]. \quad (5.13)$$

Equating the coefficients of  $\Psi_n$ , the solution is

$$v^k(y) = v_{N+1} \Psi_{N+1} + v_{N-1} \Psi_{N-1}, \quad (5.14)$$

where

$$v_{N+1} = \frac{1}{2} Q_0 \frac{1 + ik\alpha^{-1}}{2N + 3 + k^2 + \alpha^2 - ik\alpha^{-1}}, \tag{5.15a}$$

$$v_{N-1} = -NQ_0 \frac{1 - ik\alpha^{-1}}{2N - 1 + k^2 + \alpha^2 - ik\alpha^{-1}}. \tag{5.15b}$$

Using the first row of (5.7), the solution for  $\Phi^k$  is

$$\begin{aligned} \Phi^k &= \frac{1}{2} R_- v_{N+1} \Psi_{N+2} + [-(N + 1)R_+ v_{N+1} + R_0 Q_0 + \frac{1}{2} R_- v_{N-1}] \Psi_N \\ &\quad - (N - 1)R_+ v_{N-1} \Psi_{N-2}, \end{aligned} \tag{5.16}$$

for  $N = 0, 1$ , where  $\Psi_{-2} = \Psi_{-1} \equiv 0$ , and

$$R_0 = \frac{\alpha}{\alpha^2 + k^2}, \quad R_{\pm} = \frac{\alpha \pm ik}{\alpha^2 + k^2}. \tag{5.17a,b}$$

Recall that  $\alpha$  is real, so the denominators in the above expressions do not vanish. Finally, using (5.6a), the solution for  $u^k$  is

$$\begin{aligned} u^k &= \frac{1}{2} R_- v_{N+1} \Psi_{N+2} + \left[ (N + 1)R_+ v_{N+1} - \frac{ik}{\alpha} R_0 Q_0 + \frac{1}{2} R_- v_{N-1} \right] \Psi_N \\ &\quad + (N - 1)R_+ v_{N-1} \Psi_{N-2}. \end{aligned} \tag{5.18}$$

Substituting (5.12), (5.14), (5.18) and (5.16) into (5.6a–c) confirms that they are indeed the sought solutions for any values of  $k$  and  $\alpha$ .

The convergence of the Matsuno–Gill model on the sphere to the Matsuno–Gill model on the  $\beta$ -plane was shown in figures 4 and 5, for  $\epsilon^{1/2} = 10^2$ ,  $N = 0$ ,  $m = 5$  ( $k = 0.5$ ) and  $\gamma = 1$  ( $\alpha = 0.1$ , not 0.2 as in Matsuno 1966). We can now quantify the convergence in the rest of the  $(\gamma, \epsilon^{1/2})$  plane. Figure 6 shows the relative differences between the analytic approximations in (5.14), (5.16) and (5.18), and the numeric solutions as functions of  $\gamma$  and  $\epsilon^{1/2}$ . The differences were calculated as in (5.1) and are shown in logarithmic scale. Darker shades (smaller values) indicate better agreement between the analytic and numeric approximations. For the sake of comparison with the other approximations obtained in § 5, the error scales in all subsections are identical (hence the colours in this figure are under-saturated). For example, the  $(-1)$  contour, corresponding to value 0.1, is emphasized in the figure by the white dashed lines. It can be seen that the  $\beta$ -plane approximation improves gradually with increasing  $\epsilon^{1/2}$ , and becomes accurate for fast rotation rates. As we have seen in § 4, these cases correspond to the equatorial solution regime. Hence, generally speaking (and unsurprisingly), the equatorial  $\beta$ -plane approximation is valid for the equatorial solution regime.

The  $\beta$ -plane approximation for moderate damping and fast-to-slow rotation is shown in figure 7 (black contours), compared to the numeric solutions of the Matsuno–Gill model (shadings). The comparison is shown for the MRG wave-5 response: the black contours in the leftmost column correspond to the forcing in (5.12), confirming that the geopotential height of the MRG wave-5 under fast rotation can be approximated by a single Hermite function (the same was confirmed for the Kelvin wave-5 forcing in figure 4(a) and is also true for wave-1 forcing). The approximation breaks down, however, for moderate or slow rotation, as expected (figures 7b,c).

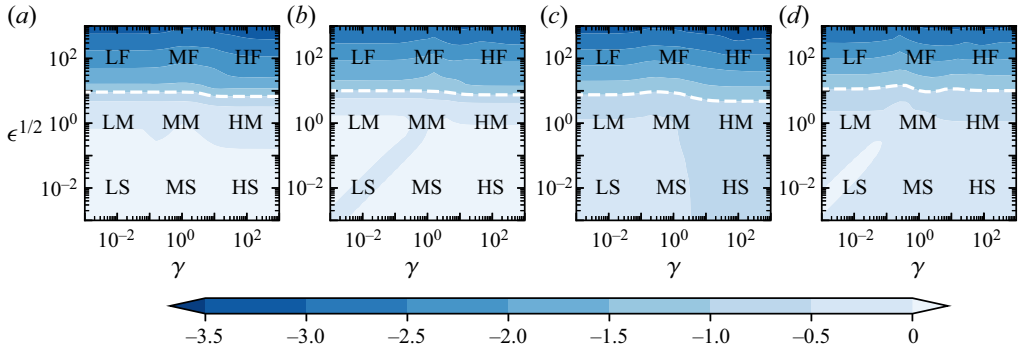


Figure 6. The relative difference defined in (5.1) between the  $\beta$ -plane approximation in (5.14), (5.16) and (5.18), and the numeric solutions obtained as described in § 4. The differences are shown in logarithmic scale. Smaller values (darker shades) indicate better agreement. For example, the  $-1$  contour, corresponding to value 0.1, is emphasized by the white dashed lines. For the sake of comparison with the other approximations obtained in § 5, the error scales in all subsections are identical. The particular samples of the  $(\gamma, \epsilon^{1/2})$  plane defined in table 1 are also marked on the figure. (a) Kelvin 5, (b) MRG 5, (c) Kelvin 1, (d) MRG 1.

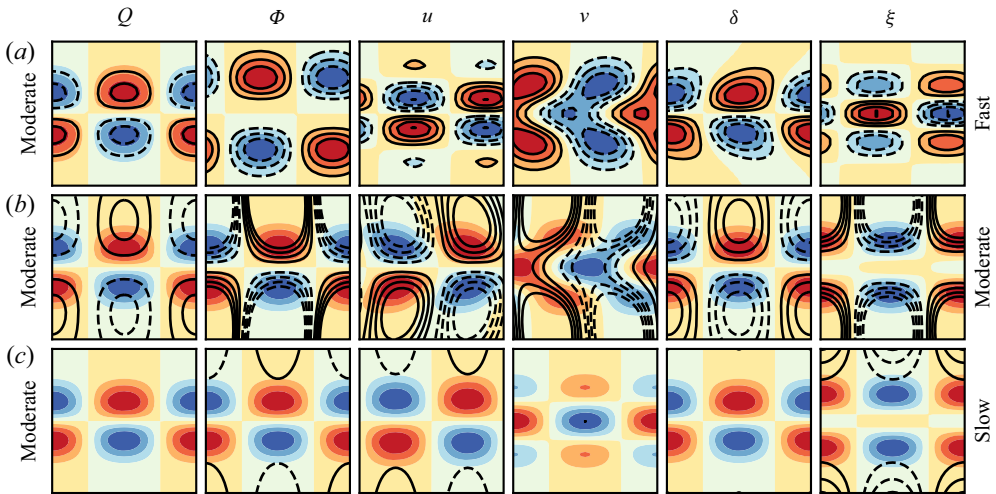


Figure 7. The  $\beta$ -plane approximation in (5.14)–(5.18) (black contours) superimposed on the steady response to an MRG wave-5 forcing (shadings). The comparison is shown for a subset of figure 3 including (a) moderate damping and fast rotation (MF), (b) moderate damping and moderate rotation (MM), and (c) moderate damping and slow rotation (MS). For the sake of clarity, the meridional domain of the equatorial regime in (a) zooms in on  $[-20^\circ, 20^\circ]$ .

### 5.2. The radiative relaxation approximation

In § 4, we observed that for heavy damping, the forcing in the continuity equation is nearly balanced by the dissipation term, with only a negligible contribution of the divergence. For  $\gamma \neq 0$ , we can rewrite the forcing as  $Q = \gamma\Phi$ , in which case the combination of the dissipation and forcing terms on the right-hand side of the continuity equation plays the role of a relaxation term  $-\gamma(\Phi - \tilde{\Phi})$ , with relaxation time  $1/\gamma$ . Hence this approximation can be thought of as a case where the geopotential height is relaxed towards the applied forcing. This is in contrast to light damping, where the forcing in the continuity equation is nearly balanced by the divergence term, and the geopotential height is far from the

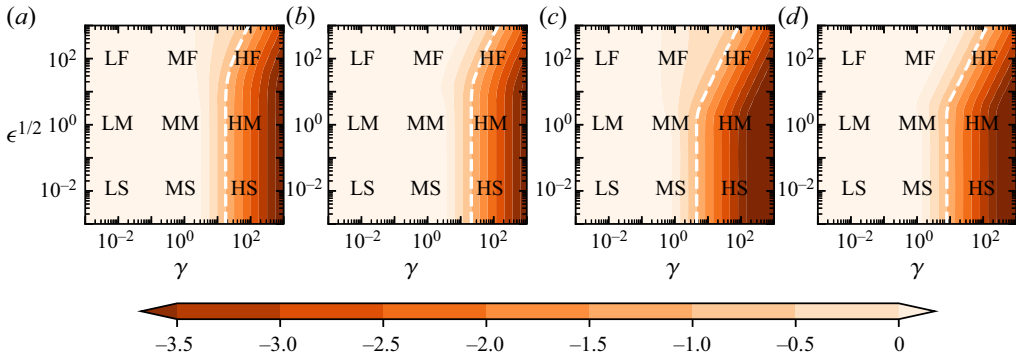


Figure 8. The relative difference defined in (5.1) between the radiative approximation in (5.19) and (5.21), and the numeric solutions obtained as described in § 4. The differences are shown in logarithmic scale. Smaller values (darker shades) indicate better agreement. For example, the  $-1$  contour, corresponding to value 0.1, is emphasized by the white dashed lines. For the sake of comparison with the other approximations obtained in § 5, the error scales in all subsections are identical. The particular samples of the  $(\gamma, \epsilon^{1/2})$  plane defined in table 1 are also marked on the figure. (a) Kelvin 5, (b) MRG 5, (c) Kelvin 1, (d) MRG 1.

applied forcing. We proceed by setting the dissipation term in the continuity equation (2.5c) equal to the forcing. The resulting approximation for the geopotential height is

$$\Phi = \gamma^{-1}Q. \tag{5.19}$$

Substituting (5.19) into (2.5a) and (2.5b) yields the following second-order algebraic system for the horizontal velocity components:

$$\begin{bmatrix} \gamma & -\epsilon^{1/2} \sin \phi \\ \epsilon^{1/2} \sin \phi & \gamma \end{bmatrix} \begin{bmatrix} u^m \\ v^m \end{bmatrix} = -\frac{1}{\gamma} \begin{bmatrix} \frac{im}{\cos \phi} Q^m \\ \frac{dQ^m}{d\phi} \end{bmatrix}. \tag{5.20}$$

For real  $\gamma, \epsilon \neq 0$ , this system has a non-vanishing determinant. Its unique solution is

$$u^m = -\frac{1}{\gamma^2 + \epsilon \sin^2 \phi} \left[ \frac{im}{\cos \phi} Q^m + \frac{\epsilon^{1/2}}{\gamma} \sin \phi \frac{dQ^m}{d\phi} \right], \tag{5.21a}$$

$$v^m = \frac{1}{\gamma^2 + \epsilon \sin^2 \phi} \left[ \frac{im\epsilon^{1/2}}{\gamma} \tan \phi Q^m - \frac{dQ^m}{d\phi} \right]. \tag{5.21b}$$

Figure 8 shows the relative difference between the radiative relaxation approximation in (5.19) and (5.21a,b), and the numeric solutions as a function of  $\gamma$  and  $\epsilon^{1/2}$ . Indeed, the radiative relaxation approximation converges to the solutions of the Matsuno–Gill model on the sphere for heavy damping (albeit less so with fast rotation). The radiative relaxation approximation for the MRG wave-5 response with light-to-heavy damping and moderate rotation is shown in figure 9 (black contours), compared to the numeric solutions of the Matsuno–Gill model (shadings). As expected, the approximate solution and the exact solution match for heavy damping and diverge for light damping. For moderate damping, the spatial distributions of the solutions agree, but their magnitudes differ.

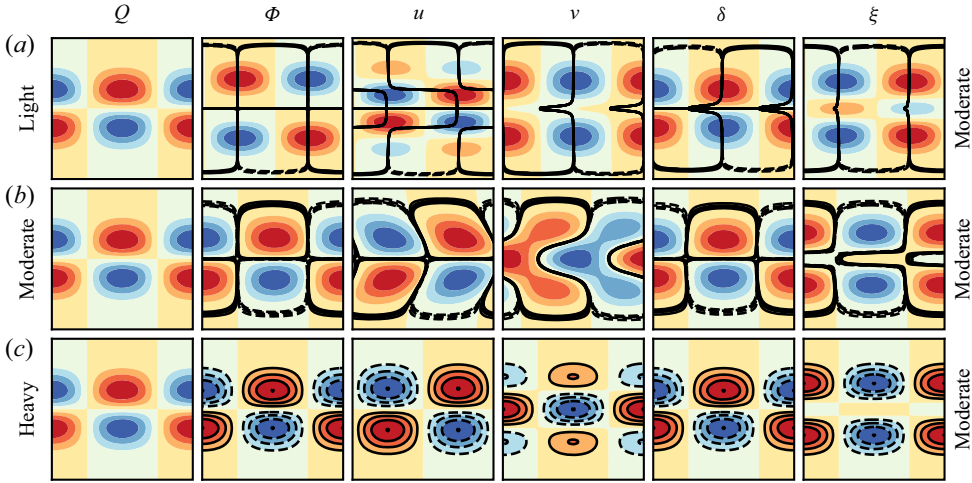


Figure 9. The radiative relaxation approximation in (5.19)–(5.21) (black contours) superimposed on the steady response to an MRG wave-5 forcing (shadings). The comparison is shown for a subset of figure 3 including (a) light damping and moderate rotation (LM), (b) moderate damping and moderate rotation (MM), and (c) heavy damping and moderate rotation (HM).

### 5.3. The geostrophic approximation

In § 4, we observed that the solutions of the Matsuno–Gill model with light damping and fast-to-moderate rotation rates are in geostrophic balance. We use this result to obtain additional simple solutions of the Matsuno–Gill model on the sphere. To this end, we set  $\gamma = 0$  in (2.5a–c), which yields a balance between the Coriolis and pressure gradient terms in the momentum equations, and between the divergence and applied forcing in the continuity equation. The resulting equations correspond to the zero-order approximation of the Matsuno–Gill model in powers of  $\gamma$ , and are given by

$$-\epsilon^{1/2} v^m \sin \phi + \frac{im}{\cos \phi} \Phi^m = 0, \tag{5.22a}$$

$$\epsilon^{1/2} u^m \sin \phi + \frac{d\Phi^m}{d\phi} = 0, \tag{5.22b}$$

$$\frac{1}{\cos \phi} \left[ imu^m + \frac{d}{d\phi} (v^m \cos \phi) \right] = Q^m. \tag{5.22c}$$

Using (5.22b) and (5.22a) to substitute  $u^m$  and  $v^m$  in (5.22c), the derivative terms containing  $d\Phi^m/d\phi$  cancel out, leaving the following algebraic relation between the geopotential and the prescribed forcing:

$$\Phi^m = \epsilon^{1/2} \frac{i}{m} \sin^2 \phi Q^m. \tag{5.23}$$

Substituting (5.23) back into (5.22b) and (5.22a) yields the corresponding horizontal velocity components

$$u^m = -2 \frac{i}{m} \cos \phi Q^m - \frac{i}{m} \sin \phi \frac{dQ^m}{d\phi} \tag{5.24}$$

and

$$v^m = -\tan \phi Q^m. \tag{5.25}$$



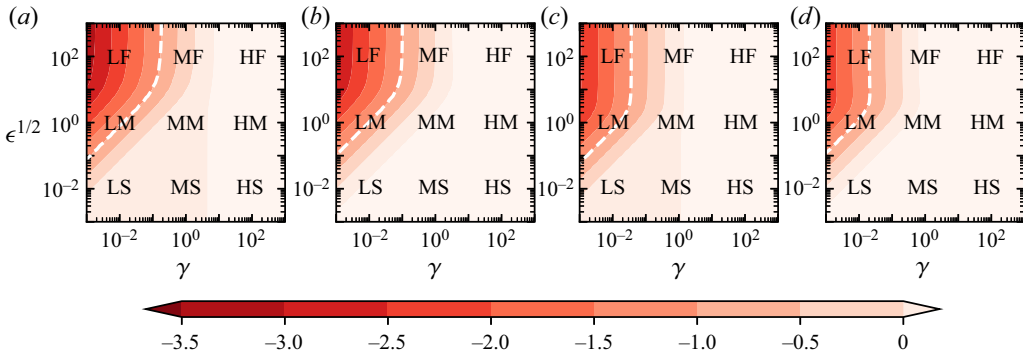


Figure 10. The relative difference defined in (5.1) between the geostrophic approximation in (5.23)–(5.25), and the numeric solutions obtained as described in § 4. The differences are shown in logarithmic scale. Smaller values (darker shades) indicate better agreement. For example, the  $-1$  contour, corresponding to value 0.1, is emphasized by the white dashed lines. For the sake of comparison with the other approximations obtained in § 5, the error scales in all subsections are identical. The particular samples of the  $(\gamma, \epsilon^{1/2})$  plane defined in table 1 are also marked on the figure. (a) Kelvin 5, (b) MRG 5, (c) Kelvin 1, (d) MRG 1.

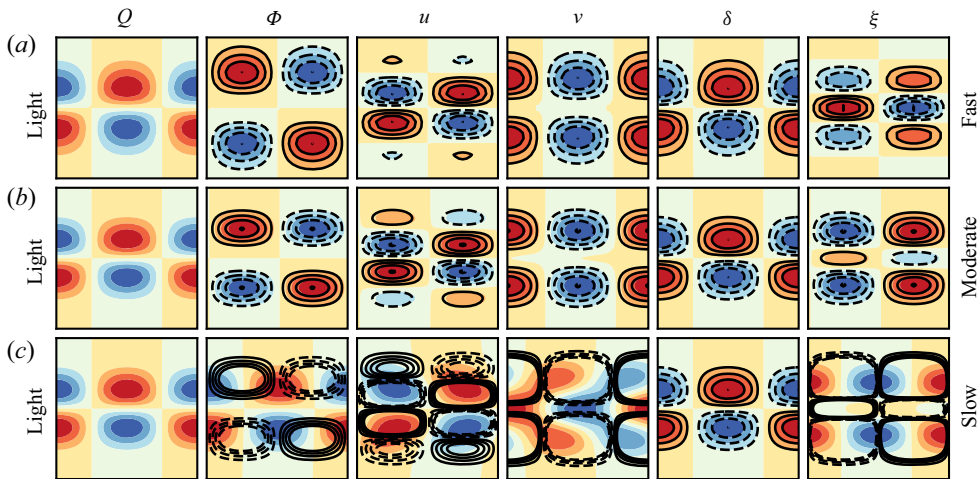


Figure 11. The geostrophic approximation in (5.23)–(5.25) (black contours) superimposed on the steady response to an MRG wave-5 forcing (shadings). The comparison is shown for a subset of figure 3 including (a) light damping and fast rotation (LF), (b) light damping and moderate rotation (LM), and (c) light damping and slow rotation (LS). For the sake of clarity, the meridional domain of the equatorial regime in (a) zooms in on  $[-20^\circ, 20^\circ]$ .

Figure 10 shows the relative difference between the geostrophic approximation in (5.23)–(5.25), and the numeric solutions as a function of  $\gamma$  and  $\epsilon^{1/2}$ . Indeed, the geostrophic approximation converges to the solutions of the Matsuno–Gill model on the sphere for light damping and moderate-to-fast rotation (LM and LF). The geostrophic approximation of the MRG wave-5 response in these two cases, as well as for light damping and slow rotation (LS), is shown in figure 11 (black contours), compared to the numeric solutions of the Matsuno–Gill model (shadings).

The geostrophic approximation in (5.23)–(5.25) corresponds to the zero-order approximation of the Matsuno–Gill model on the sphere in powers of  $\gamma$  (see § 4.2 in the supplementary material). Adding the first-order terms improves the accuracy within

the identified region in figure 10, but barely expands this region. The reason is that the solutions outside the LM and LF regions are highly a-geostrophic (as we observed in § 4).

5.4. The non-rotating approximation

The non-rotating approximation reduces the order of the RSWEs from third order to second order in time (i.e. no Rossby waves) by setting the non-dimensional rate of rotation equal to zero, yielding the canonical wave equation. Similarly, setting  $\epsilon^{1/2} = 0$  in the Matsuno–Gill model (2.5a–c) yields

$$\frac{im}{\cos \phi} \Phi^m = -\gamma u^m, \tag{5.26a}$$

$$\frac{d\Phi^m}{d\phi} = -\gamma v^m, \tag{5.26b}$$

$$\frac{1}{\cos \phi} \left[ imu^m + \frac{d}{d\phi}(v^m \cos \phi) \right] = -\gamma \Phi^m + Q^m. \tag{5.26c}$$

Using (5.26b) and (5.26a) to substitute  $u^m$  and  $v^m$  in (5.26c) yields the following boundary value problem for the geopotential in terms of the specified forcing:

$$\Delta^m \Phi^m = \gamma^2 \Phi^m - \gamma Q^m, \tag{5.27}$$

where  $\Delta^m$  is the  $m$ -restricted Laplacian defined as

$$\Delta^m = \frac{1}{\cos \phi} \left[ \frac{d}{d\phi} \left( \cos \phi \frac{d}{d\phi} \right) - \frac{m^2}{\cos \phi} \right]. \tag{5.28}$$

Equation (5.27) can be solved by expanding both  $\Phi^m$  and  $Q^m$  in series of associated Legendre polynomials (ALPs), which are the eigenfunctions of the  $m$ -restricted Laplacian in (5.28). Specifically, let  $P_l^m$  denote the ALP of degree  $l$  and order  $m$ ; then

$$\Delta^m P_l^m(\sin \phi) = -l(l+1)P_l^m(\sin \phi). \tag{5.29}$$

Fortunately, for  $\epsilon^{1/2} \rightarrow 0$ , the geopotential height field associated with the Kelvin and MRG waves can be approximated accurately by a single ALP. Thus we proceed to find non-rotating solutions of the Matsuno–Gill model in response to the following prescribed forcing:

$$Q^m(\phi) = Q_f^m P_l^m(\sin \phi), \tag{5.30}$$

where  $Q_f^m$  is a constant amplitude, and  $l = m$  or  $l = m + 1$  for Kelvin or MRG waves, respectively. Substituting (5.30) into (5.27) and using (5.29), the solution for  $\Phi^m$  in the non-rotating approximation is

$$\Phi^m = \frac{\gamma}{\gamma^2 + l(l+1)} Q_f^m P_l^m(\sin \phi). \tag{5.31}$$

Using (5.26a) and (5.26b), the corresponding solutions for  $u^m$  and  $v^m$  in the non-rotating approximation are

$$u^m = -\frac{im}{\gamma^2 + l(l+1)} \frac{Q_f^m}{\cos \phi} P_l^m(\sin \phi) \tag{5.32}$$

and

$$v^m = -\frac{1}{\gamma^2 + l(l+1)} Q_f^m \frac{dP_l^m(\sin \phi)}{d\phi}. \tag{5.33}$$

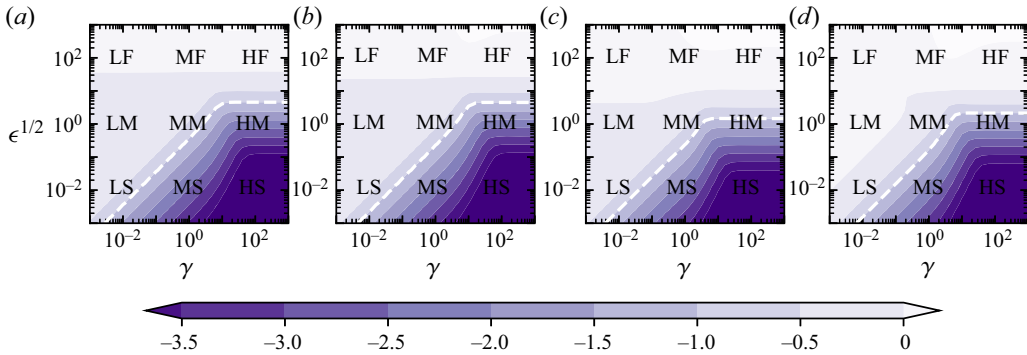


Figure 12. The relative difference defined in (5.1) between the non-rotating approximation in (5.31)–(5.33), and the numeric solutions obtained as described in § 4. The differences are shown in logarithmic scale. Smaller values (darker shades) indicate better agreement. For example, the  $-1$  contour, corresponding to value 0.1, is emphasized by the white dashed lines. For the sake of comparison with the other approximations obtained in § 5, the error scales in all subsections are identical. The particular samples of the  $(\gamma, \epsilon^{1/2})$  plane defined in table 1 are also marked on the figure. (a) Kelvin 5, (b) MRG 5, (c) Kelvin 1, (d) MRG 1.

Figure 12 shows the relative difference between the non-rotating approximation in (5.31)–(5.33), and the numeric solutions as a function of  $\gamma$  and  $\epsilon^{1/2}$ . As expected, the non-rotating approximation converges to the solutions of the Matsuno–Gill model on the sphere for moderate-to-heavy damping and slow rotation (MS and HS). In addition, the non-rotating approximation can also approximate the solution for heavy damping and moderate rotation (HM). The non-rotating approximation for the MRG wave-5 response with slow rotation (and all damping rates) is shown in figure 13 (black contours), compared to the numeric solutions of the Matsuno–Gill model (shadings). Importantly, the black contours in the leftmost column correspond to forcing in (5.30), confirming the assumption that the geopotential height of the MRG wave can be approximated by a single ALP (the same is also true for the Kelvin wave). Finally, the vorticity in this approximation is identically zero, while the vorticity at moderate damping and slow rotation (MS) is far from small.

The non-rotating approximation in (5.31)–(5.33) corresponds to the zero-order approximation of the Matsuno–Gill model on the sphere in powers of  $\epsilon^{1/2}$  (see § 4.3 in the supplementary material). Adding the first-order terms improves the accuracy within the identified region in figure 12, but barely expands this region. As we will see in § 7, the solutions outside the HM and HS regions are qualitatively different from non-rotating in terms of the excited waves.

### 5.5. The weak temperature gradient approximation

The accuracy of the geostrophic and non-rotating approximations is reduced at light damping and slow rotation. The reason is that, as established by Neelin (1988) and Bretherton & Sobel (2003), the Matsuno–Gill model becomes underdetermined when  $\gamma = \epsilon^{1/2} = 0$ . Specifically, the momentum equations mandate that  $\Phi^m \equiv 0$  in that case, but the continuity equation mandates only that  $\delta^m = Q^m$ . Any combination of  $u^m$  and  $v^m$  that satisfies the last condition will therefore be a solution. As an alternative, Bretherton & Sobel (2003) studied the weak temperature gradient (WTG) approximation, where the dissipation term in the continuity equation is negligible compared to the divergence and forcing terms. Bretherton & Sobel (2003) studied the WTG approximation for the

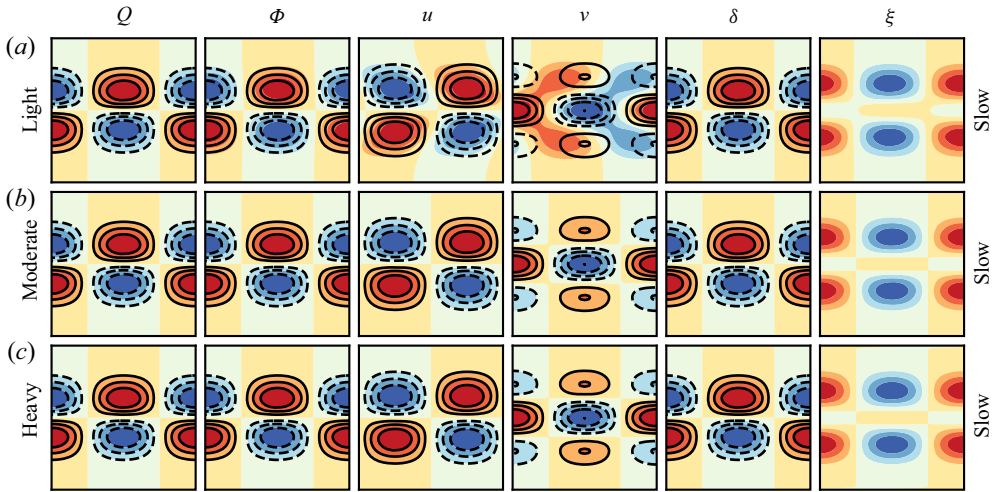


Figure 13. The non-rotating approximation in (5.31)–(5.33) (black contours) superimposed on the steady response to an MRG wave-5 forcing (shadings). The comparison is shown for a subset of figure 3 including (a) light damping and slow rotation (LS), (b) moderate damping and slow rotation (MS), and (c) heavy damping and slow rotation (HS).

Matsuno–Gill model on the equatorial  $\beta$ -plane. Our observations in § 4 show that this idea is also relevant here; as we have seen, with light damping, the forcing in the continuity equation is balanced by the divergence term, while the contribution of the dissipation term is negligible. Thus we now examine the WTG approximation for the Matsuno–Gill model on the sphere. This approximation yields no analytic simplification; we can only examine it numerically.

Figure 14 shows the relative difference between the WTG approximation and full model solutions as a function of  $\gamma$  and  $\epsilon^{1/2}$ . Indeed, the WTG approximation matches the full model with light damping and slow rotation (LS), and is also ‘visually accurate’ for light damping and fast rotation (LF), light damping and moderate rotation (LM), moderate damping and slow rotation (MS), and, most notably, moderate damping and moderate rotation (MM).

The WTG approximation for the MRG wave-5 response in the HF, MM and LS cases is shown in figure 15 (black contours), compared to the numeric solutions of the Matsuno–Gill model (shadings). As observed in figures 2 and 3, the solutions for the LS and MM cases are similar, but not identical (in terms of the magnitudes of the fields). Finally, Bretherton & Sobel (2003) found that the Matsuno–Gill model under the WTG approximation has a far-field response, in the sense that the steady-state geopotential in response to an equatorially trapped forcing is not itself equatorially trapped. The situation for the Matsuno–Gill model on the sphere is somewhat different. With light damping and slow rotation, where the WTG approximation is most accurate, the extension of the forcing is no longer equatorially trapped. The WTG also provides an accurate approximation for light damping and fast rotation, where both the forcing and the response are equatorially trapped.

### 5.6. The long-wave approximation

For the sake of comparison with Gill (1980), we now examine the long-wave approximation where the dissipation term in the  $v$ -momentum equation is negligible,

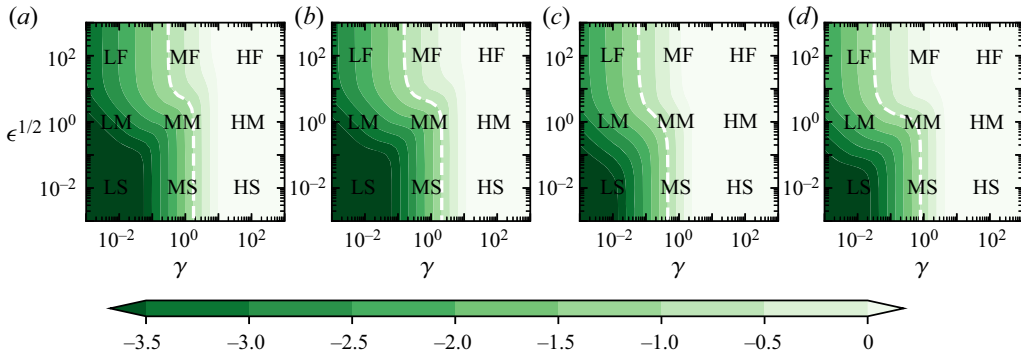


Figure 14. The relative difference defined in (5.1) between the WTG approximation and Matsuno–Gill model solutions obtained as described in § 4. The differences are shown in logarithmic scale. Smaller values (darker shades) indicate better agreement. For example, the  $-1$  contour, corresponding to value 0.1, is emphasized in the figure by the white dashed lines. For the sake of comparison with other approximations obtained in § 5, the error scales in all subsections are identical. The particular samples of the  $(\gamma, \epsilon^{1/2})$  plane defined in table 1 are also marked on the figure. (a) Kelvin 5, (b) MRG 5, (c) Kelvin 1, (d) MRG 1.

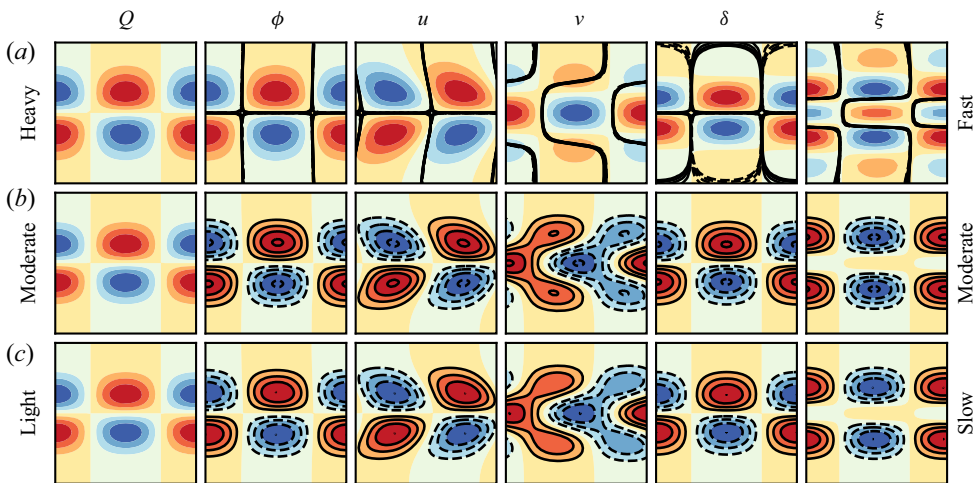


Figure 15. The WTG approximation (black contours) superimposed on the steady response to an MRG wave-5 forcing (shadings). The comparison is shown for a subset of figure 3 including (a) heavy damping and fast rotation (HF), (b) moderate damping and moderate rotation (MM), and (c) light damping and slow rotation (LS). For the sake of clarity, the meridional domain of the equatorial regime in (a) zooms in on  $[-20^\circ, 20^\circ]$ .

compared to the Coriolis and pressure gradient terms. This approximation is not motivated by any of our observations in § 4, suggesting that additional assumptions are necessary for this approximation to hold on the sphere, in addition to the ones imposed by Gill (1980) on the equatorial  $\beta$ -plane. Yet, as we will see in § 6, it does improve on the geostrophic approximation for light damping and fast rotation, consistent with the fact that it is a less constrained version of the geostrophic approximation, where only the zonal wind is in geostrophic balance. Like the WTG approximation, this approximation yields no analytic simplification; we can only examine it numerically.

Figure 16 shows the relative difference between the long-wave approximation and Matsuno–Gill model solutions as a function of  $\gamma$  and  $\epsilon^{1/2}$ . The long-wave approximation



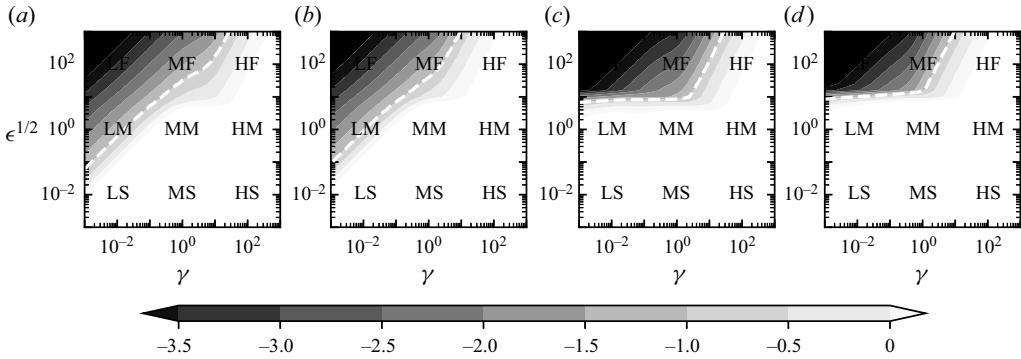


Figure 16. The relative difference defined in (5.1) between the long-wave approximation and Matsuno–Gill model solutions obtained as described in § 4. The differences are shown in logarithmic scale. Smaller values (darker shades) indicate better agreement. For example, the  $-1$  contour, corresponding to value 0.1, is emphasized in the figure by the white dashed lines. For the sake of comparison with the other approximations obtained in § 5, the error scales in all subsections are identical. The particular samples of the  $(\gamma, \epsilon^{1/2})$  plane defined in table 1 are also marked on the figure. (a) Kelvin 5, (b) MRG 5, (c) Kelvin 1, (d) MRG 1.

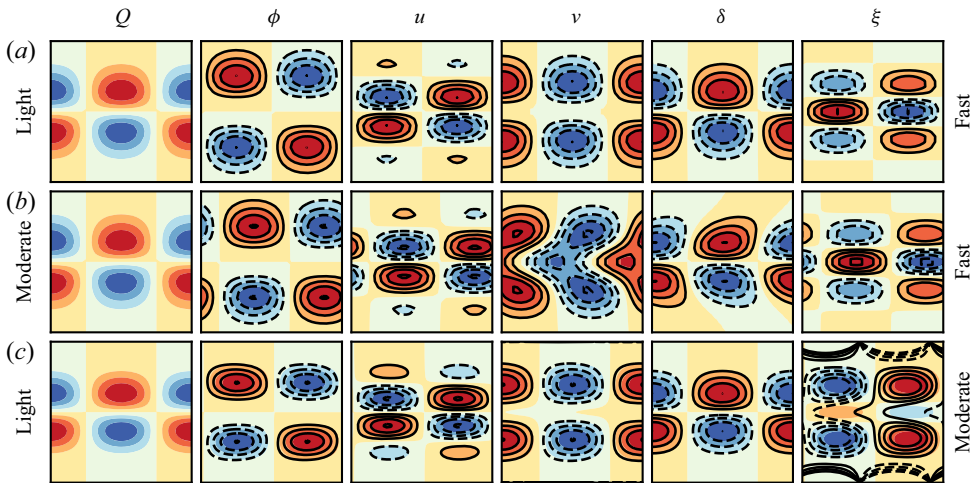


Figure 17. The long-wave approximation (black contours) superimposed on the steady response to an MRG wave-5 forcing (shadings). The comparison is shown for a subset of figure 3 including (a) light damping and fast rotation (LF), (b) moderate damping and fast rotation (MF), and (c) light damping and moderate rotation (LM). For the sake of clarity, the meridional domain of the equatorial regime in (a,b) zooms in on  $[-20^\circ, 20^\circ]$ .

converges to the full model at light damping and fast rotation. It is also ‘visually accurate’ for moderate damping and fast rotation, and to a lesser degree (only for the wave-5 response) for light damping and moderate rotation. The long-wave approximation for the MRG wave-5 response in these three cases is shown in figure 17 (black contours), compared to the numeric solutions of the Matsuno–Gill model (shadings). Indeed, it is less accurate for light damping and moderate rotation, in the sense that  $\Phi$  and  $u$  (and  $\delta$ ) are approximated accurately, but  $v$  and  $\xi$  are not.



## 6. Applicability to Earth, Venus and Titan

We now consider our results in the context of the atmospheres and oceans of Earth and other planets, in particular with regard to the simple solutions obtained above. For example, steady motion on Earth is generally believed to be near geostrophic balance, but, as we have seen in § 5.3, the steady solutions of the forced-dissipated RSWEs are in geostrophic balance only in a small subset of the  $(\gamma, \epsilon^{1/2})$  plane. In general, the  $\beta$ -plane, radiative relaxation, geostrophic and WTG approximations are all believed to be relevant to Earth, but capture the solutions of the forced-dissipated RSWEs only in subsets of the  $(\gamma, \epsilon^{1/2})$  plane.

Figure 18 shows the most accurate approximation, compared to the numeric solutions, as a function of  $\gamma$  and  $\epsilon^{1/2}$ . At each point in the  $(\gamma, \epsilon^{1/2})$  plane, we check for which of the six approximations the relative difference defined in (5.1) is smallest, and whether its value is smaller than or equal to 0.1. The latter condition is added to ensure that the best approximation is a good one. There are important caveats to this figure. First, the value 0.1 is subjective; it is possible to extend the regions of validity of each approximation by considering e.g. value 0.2, but only to a small extent since the solutions soon become qualitatively different. Second, as is evident from figures 6, 8, 10, 12, 14 and 16, there are overlaps between different approximations. For example, the radiative relaxation and non-rotating approximations both capture the solutions at heavy damping and slow rotation. Third, the most accurate approximation may not be the most appropriate one. For example, the WTG and long-wave approximations are not analytic. Depending on the desired accuracy, it may be preferable to use the simpler (analytic), but less accurate, geostrophic approximation in the regions of light damping and moderate-to-fast rotation. Note that the geostrophic approximation is included in the figure, but its accuracy is less than that of either the WTG or the long-wave approximation at every point in the  $(\gamma, \epsilon^{1/2})$  plane. Considering these caveats, the purpose of this figure is to provide a qualitative overview. Perhaps the key observation is that most of the points in the  $(\gamma, \epsilon^{1/2})$  plane can be treated with some simplified version of the Matsuno–Gill model.

The dashed rectangles in figures 18(a–c) indicate the estimated regions of relevance to Earth’s troposphere, stratosphere and ocean, respectively. Using the mean radius, gravitational acceleration, and angular frequency of the Earth, the remaining unknown in the Lamb number  $\epsilon = (2\Omega a)^2/gH$  is the mean layer thickness  $H$  of the shallow-water model. The rectangles shown in figure 18 correspond to values of  $H$  between the barotropic mode and first baroclinic mode in each case. The values of  $H$  in the atmosphere are based on the results of De-Leon, Paldor & Garfinkel (2020), who estimated the ‘equivalent depth’ for different background temperature profiles and boundary conditions. For the troposphere, we take  $H$  to be between 10 km and 100 m. For the stratosphere, we take  $H$  to be between 9 km and 3.5 km. For the ocean, we take  $H$  to be between 4 km and 0.5 m. The first number is based on the mean ocean depth, and the second number on the estimations of Chelton *et al.* (1998). For the damping coefficient, we use values between  $0.1 \text{ day}^{-1}$  and  $1 \text{ day}^{-1}$ . Since the time scale introduced in § 2 involves  $H$ , the non-dimensional damping coefficients  $\gamma$  (the rectangles’ widths) in figures 18(a–c) are different, even though the dimensional values are the same in all cases. Due to the logarithmic scale on both axes, slightly different estimations of the parameter lead to only small changes in the rectangle. Hence we argue that they are fairly representative of the troposphere, stratosphere and ocean.

Approximately half of the troposphere-relevant region is well approximated by the  $\beta$ -plane approximation, where it is also close to the region of the plane corresponding

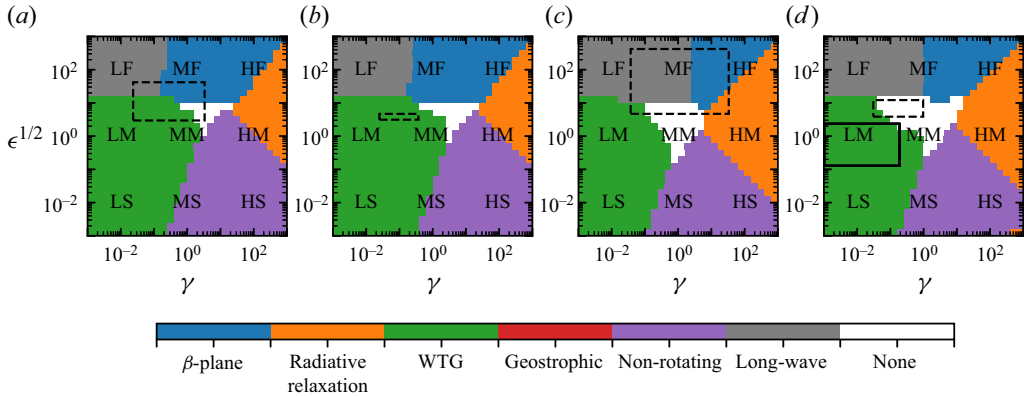


Figure 18. A comparison between the  $\beta$ -plane, radiative relaxation, geostrophic, non-rotating, WTG and long-wave approximations. At each point of the  $(\gamma, \epsilon^{1/2})$  plane, the comparison is made by checking for which of the four approximations the relative difference defined in (5.1) is smallest, and whether its value is smaller than or equal to 0.1. The particular samples of the  $(\gamma, \epsilon^{1/2})$  plane defined in table 1 are also marked on the figure. Dashed rectangles in (a–c) indicate the regions relevant to Earth’s troposphere, stratosphere and ocean, respectively, while the dashed and solid rectangles in (d) indicate the regions relevant to the tropospheres of Venus and Titan, respectively. (a) Kelvin 5, (b) MRG 5, (c) Kelvin 1, (d) MRG 1.

to the original results obtained by Matsuno and Gill (the MF region). On the other hand, approximately half of the troposphere relevant region is also qualitatively different from the  $\beta$ -plane approximation, and is more accurately approximated by the WTG approximation. The stratosphere-relevant region is also qualitatively different from the  $\beta$ -plane approximation, and is more accurately approximated by the WTG approximation. Finally, the ocean-relevant region is, for all practical matters, covered by the original results of Matsuno and Gill, with or without the long-wave approximation.

In addition to our own planet Earth, the Matsuno–Gill model may also be of interest for the atmospheres of Venus and Titan, which are characterized by global-scale Hadley circulations and strong equatorial waves that flux westerly momentum towards the equator (Svedhem *et al.* 2007; Mitchell *et al.* 2011; Yamamoto 2019; Peralta *et al.* 2020). The dashed and solid rectangles in figure 18(d) indicate the estimated region of relevance to the tropospheres of Venus and Titan, respectively. For Venus, the range of  $\epsilon$  used here is taken from Yamamoto (2019) to be  $\epsilon^{1/2} = 11\text{--}160$ , which in turn is based on different estimations of the speed of gravity waves in Venus’ troposphere. For Titan, the upper limit of  $\epsilon$  used here is taken from Yamamoto (2019) to be  $\epsilon^{1/2} = 5.5$ , corresponding to  $H = 75$  m. For the lower limit, we take  $H = 25$  km, corresponding to  $\epsilon^{1/2} = 0.016$ . This choice is based on the observation that the ‘equivalent depth’ of the barotropic mode tends to be of the same order of magnitude as the scale height, which is  $H = 15\text{--}50$  km for Titan (Müller-Wodarg *et al.* 2014). For the damping coefficient, we use values between 0.1 and 1 of the planet’s period of rotation, as we did for Earth: specifically,  $4.12 \times 10^{-4}\text{--}4.12 \times 10^{-3}$  day $^{-1}$  for Venus, and  $6.25 \times 10^{-3}\text{--}6.25 \times 10^{-2}$  day $^{-1}$  for Titan.

The Venusian atmosphere is poorly characterized by most of these approximations. Specifically, it falls within the region poorly described by all approximations for wavenumber 1 for either the mixed Rossby–gravity mode or the Kelvin mode. For higher wavenumbers, the WTG approximation is somewhat better. However, the degree of success is sensitive to the precise value of damping used (which is poorly constrained

by observations). The relative lack of success for Venus is consistent with observations showing a substantial meridional velocity for wavenumber 1 Kelvin waves in Venus’ atmosphere (Belton *et al.* 1976; Covey & Schubert 1982; Del Genio & Rossow 1990; Smith, Gierasch & Schinder 1992; Yamamoto 2019; Peralta *et al.* 2020) that cannot be described by the Matsuno–Gill  $\beta$ -plane model of a fast rotating atmosphere.

Titan’s atmosphere is well represented by the WTG approximation. The geostrophic approximation also works in the region of relevance to Titan, and while it is less accurate than the WTG, it is analytic. A non-zero meridional component of an equatorial Kelvin(-like) wave is seen in a Titan general circulation model as well (Mitchell *et al.* 2011). This Kelvin wave part of the solution can be described by the *ad hoc* solution of Garfinkel *et al.* (2017), which has a functional form different to the solutions of Longuet-Higgins (1968) and Matsuno (1966); however, this solution applies only to the Kelvin wave and not to other wave modes.

### 7. Wave spectrum

A key feature of the analysis of Gill (1980) is the description of the steady circulation in terms of the constituent waves. In the absence of analytic solutions of the Matsuno–Gill model on the sphere for arbitrary values of  $\gamma$  and  $\epsilon$ , we proceed to find the constituent waves numerically by projecting the solutions on the spectrum of the free RSWEs. Let  $X_\omega = [u^m, v^m, \Phi^m]^T$  denote the eigensolution of the free RSWEs corresponding to the eigenvalue (frequency)  $\omega$ , obtained by solving (2.7) using the Chebyshev collocation method. Similarly, let  $X_\gamma = [u^m, v^m, \Phi^m]^T$  denote the solution vector of the Matsuno–Gill model with damping rate  $\gamma$ , obtained by solving (2.5a–c) using the Chebyshev collocation method. The projection of the latter on the former is

$$\text{projection}_\omega = \frac{(X_\omega, X_\gamma)}{(X_\omega, X_\omega)}, \tag{7.1}$$

where  $(X, \bar{X})$  is the inner product defined in (5.2). Note that the linear operator of the free RSWEs,  $\mathbf{L}$  on the left-hand side of (2.7), is skew-Hermitian with respect to the inner product in (5.2), i.e.  $(\mathbf{L}X, \bar{X}) = -(X, \mathbf{L}^*\bar{X})$ , which guarantees that eigensolutions corresponding to different frequencies are orthogonal. Having found the projections of  $X_\gamma$  on each of the resolved  $X_\omega$ , we calculate the fractional spectral power associated with each one:

$$\text{power}_\omega = \frac{|\text{projection}_\omega|^2}{\sum_\omega |\text{projection}_\omega|^2}. \tag{7.2}$$

The resulting projections of the Kelvin wave-5 forcing on the free EIG2, EIG1, EIG0, Kelvin, Rossby2, Rossby1, MRG, WIG1 and WIG2 wave modes are given in table 2(a). For the sake of comparison with the Matsuno–Gill model on the equatorial  $\beta$ -plane, we follow the classification of the free wave modes used by Matsuno. However, as noted by Garfinkel *et al.* (2017), from the point of view of the eigenvalue problem associated with the free RSWEs on the sphere, the Kelvin wave is more accurately classified as the lowest mode EIG wave.

Starting with the MF case (second row from the top), the response consists solely of the free Kelvin and Rossby1 waves, with the Kelvin wave contributing 3 % of the total power, and the Rossby1 wave contributing 97 %. The excitation of these two waves is consistent with the symmetric forcing case studied by Gill. The particular distribution is consistent with the fact that the petals of the fleur-de-lis in Matsuno’s solution are more

(a) Kelvin wave-5 response

	EIG2	EIG1	EIG0	Kelvin	Rosby2	Rosby1	MRG	WIG1	WIG2	Sum
LF	—	44 %	—	—	—	9 %	—	47 %	—	100 %
MF	—	—	—	3 %	—	97 %	—	—	—	100 %
HF	—	2 %	—	50 %	—	28 %	—	20 %	—	100 %
LM	—	3 %	—	3 %	—	79 %	—	5 %	—	90 %
MM	—	15 %	—	2 %	—	23 %	—	43 %	—	83 %
HM	—	—	—	50 %	—	—	—	49 %	—	99 %
LS	—	13 %	—	10 %	—	36 %	—	11 %	—	70 %
MS	—	3 %	—	3 %	—	57 %	—	29 %	—	92 %
HS	—	—	—	49 %	—	—	—	50 %	—	99 %

(b) MRG wave-5 response

	EIG2	EIG1	EIG0	Kelvin	Rosby2	Rosby1	MRG	WIG1	WIG2	Sum
LF	30 %	—	12 %	—	5 %	—	21 %	—	32 %	100 %
MF	—	—	2 %	—	93 %	—	5 %	—	—	100 %
HF	2 %	—	27 %	—	27 %	—	24 %	—	20 %	100 %
LM	2 %	—	1 %	—	53 %	—	32 %	—	2 %	90 %
MM	14 %	—	—	—	12 %	—	23 %	—	31 %	80 %
HM	1 %	—	48 %	—	—	—	—	—	49 %	98 %
LS	10 %	—	11 %	—	15 %	—	24 %	—	11 %	71 %
MS	3 %	—	1 %	—	40 %	—	16 %	—	29 %	89 %
HS	1 %	—	48 %	—	—	—	—	—	50 %	99 %

Table 2. Projections of the Matsuno–Gill model solutions on the free RSWEs wave modes: (a) in response to a Kelvin wave-5 forcing; (b) in response to an MRG wave-5 forcing. Reported values correspond to the percent fraction (accurate to 1 %) of the total power projected on the (columns from left to right) EIG2, EIG1, EIG0, Kelvin, Rosby2, Rosby1, MRG, WIG1 and WIG2 wave modes. The classification of the modes follows the classification used in Matsuno (1966). The combined contribution of the eight modes is given in the final column. The different rows correspond to the nine samples of the  $(\gamma, \epsilon^{1/2})$  plane given in table 1. To improve readability, 0 % projections, to the retained accuracy, are replaced by dashes.

pronounced than its stem (figure 9 in Matsuno (1966), figure 1 of the present work). As the forcing wavenumber decreases, the Kelvin wave contribution increases, becoming the main contribution only when the forcing wavenumber is smaller than 1, which is possible only on the plane (see § 4 in the supplementary material). This is consistent with the more pronounced Kelvin wave in Gill’s version of the fleur-de-lis (figure 1(b) in Gill 1980), where the localized forcing projects on smaller wavenumbers.

Continuing with the equatorial solutions regime, the LF and HF spectra are appreciably different from the MF spectrum in terms of the excited waves and their ratios, due to the different damping rates. The Kelvin wave forcing in the  $\beta$ -plane approximation is proportional to the lowest Hermite function  $\Psi_0 = \exp(-y^2/2)$ . Besides the Kelvin wave,  $\Psi_0$  appears only in the geopotential height of the EIG1, Rosby1 and WIG1 waves. Hence only these four waves can be excited, and their ratios depend on the damping rate. Indeed, the contributions of these four waves in the equatorial solution regime sum to 100 %. However, in contrast to the MF response, the LF response has no Kelvin wave contribution at all, and its main contributions come from the EIG1 (44 %) and WIG1 (47 %) waves, while the main contribution to the HF response is the Kelvin wave (50 %), with substantial contributions from the Rosby1 (28 %) and WIG1 (20 %) waves.

The reason why the ‘Kelvin’ and ‘MRG’ wave forcings excite other waves besides the Kelvin and MRG waves themselves is that the forcing consists of only the geopotential part

of those waves. A true Kelvin or MRG wave (or any other wave mode) forcing consists of the unique  $X = [u^m, v^m, \Phi^m]^T$  triplet associated with that wave, and the response of the linear Matsuno–Gill model to such a forcing would consist solely of that wave as well.

Moving on to the global solution regime, the HM and HS responses consist solely of the free Kelvin and WIG1 waves, with each contributing 50 % (within the retained accuracy) of the total power. As observed in §§ 4 and 5.2, the forcing in the HM and HS responses is nearly balanced by the dissipation term (i.e.  $-\gamma \Phi$ ), with the contribution of the divergence in the continuity equation being negligible. In addition, as observed in § 5.4, these two cases are approximated accurately by the non-rotating approximation, which consists of identical pairs of oppositely propagating gravity waves (no Rossby or MRG waves). Thus the time-independent forcing projects equally on the first eastward and westward gravity waves, manifested as the Kelvin and WIG1 waves in this limit. In contrast to the HM and HS responses, the main contributions to the MS response are the Rossby1 (57 %) and WIG1 (29 %) waves, with the Kelvin and EIG1 waves contributing only little (3 % each). However, the dissipation term in the continuity equation in that case is an order of magnitude smaller than the divergence term, and the forcing projects on the Rossby1 wave as well.

The main contribution to the LM response is the Rossby1 wave (79 %), with the Kelvin (3 %), EIG1 (3 %) and WIG1 (5 %) waves contributing only little. As we have seen in § 5.3, this case is approximated accurately by the geostrophic approximation, explaining the preferential Rossby wave excitation. Typically, the IG and Kelvin waves propagate away during geostrophic adjustment (the transient part of the solution), leaving only the Rossby waves in the long-term solution.

Our main observation regarding the MM and LS responses is the fact that the total power contained in the first nine wave modes reported in table 2 account for only 83 % and 70 %, respectively. Examining the subsequent wave modes, we find that the EIG3 and WIG3 waves account for an additional 7 % of the total power in the MM response (bringing the contribution of the first 11 waves modes up to 90 %), and 14 % of the total power in LS responses (bringing the contribution of the first 11 waves modes up to 84 %). In other words, the expansion of the response in terms of the free wave modes converges more slowly in these two cases compared to all other cases. This observation is likely a different manifestation of the difficulty associated with finding simple (analytic) approximations (excluding WTG) in these two cases.

Finally, the resulting projections of the MRG wave-5 forcing on the free EIG2, EIG1, EIG0, Kelvin, Rossby2, Rossby1, MRG, WIG1 and WIG2 wave modes are given in table 2(b). In general, the above discussion with appropriate substitutions describes this case as well. In particular, the MRG wave forcing in the  $\beta$ -plane approximation is proportional to the second-lowest Hermite function  $\Psi_1 = 2y \exp(-y^2/2)$ . Besides the MRG wave,  $\Psi_1$  appears only in the geopotential height of the EIG2, EIG0, Rossby2 and WIG2 waves. Hence only these five waves can be excited, and indeed their contributions in the equatorial solutions regime sum to 100 %. The main contribution to the MF response is the Rossby2 wave (93 %), with the EIG0 (2 %) and MRG (5 %) waves contributing only little.

The main difference between the Kelvin and MRG wave responses is in the meridional symmetry of the spectrum. The free RSWEs have a definite meridional symmetry, such that consecutive wave modes have opposite symmetries (e.g. in terms of  $\Phi^m$ ). If the forcing has a definite symmetry, then the solutions of the Matsuno–Gill model would have a definite symmetry as well. Considering that the forcing is applied via the continuity equation, it can excite only waves having the same symmetry in terms of  $\Phi^m(\phi)$ . In the

nonlinear case, however, this is not true: a purely antisymmetric forcing preferentially excites symmetric modes due to triad interactions, as discussed in detail in Garfinkel *et al.* (2021) and Shamir *et al.* (2021a,b). Garfinkel *et al.* (2021) also give theoretical justifications for the observed red background. This, in turn, might explain the prevalence of the solution identified by Matsuno and Gill, since the Kelvin and Rossby1 waves are (some of) the lowest modes.

Aside from the exploration of the  $(\gamma, \epsilon^{1/2})$  plane, the wave spectrum is the key distinction between the Matsuno–Gill model on the  $\beta$ -plane and its counterpart on the sphere. The effect of the Lamb number is to alter the eigenmodes of the free RSWEs, and therefore the waves that can be excited by a given forcing.

### 8. The response to a local forcing

As discussed in § 3, the forcing used by Matsuno (1966) and Gill (1980) corresponds to the geopotential height of the Kelvin and MRG waves. Hence a natural extension of the forcing to the sphere is the geopotential height corresponding to these two waves. A limitation of this choice, however, is the fact that the resulting forcing in the equatorial solutions regime is trapped equatorially, while the resulting forcing in the global solutions regime is global. One is often interested in the global response to a local forcing, which is the focus of this section. In addition to making the forcing meridionally localized, we also demonstrate the applicability of our results to a zonally localized forcing akin to that used by Gill (1980). Specifically, we study the response to the forcing

$$Q(\lambda, \phi) = \begin{cases} \cos(3\lambda) \exp[-(24\phi/\pi)^2/2], & \text{for } |\lambda| \leq \pi/6, \\ 0, & \text{for } |\lambda| > \pi/6. \end{cases} \quad (8.1)$$

As discussed in § 2, due to the linearity of the Matsuno–Gill model and the  $\lambda$ -independence of the coefficients, we may study each Fourier mode separately. The Fourier series of the above forcing can be obtained analytically as

$$Q(\lambda, \phi) = \sum_{m=-\infty}^{\infty} Q_0^m \exp(im\lambda) \exp[-(24\phi/\pi)^2/2], \quad (8.2)$$

where

$$Q_0^m = \begin{cases} \frac{1}{12}, & \text{for } m = \pm 3, \\ \frac{1}{2\pi} \left[ \frac{\sin\left[(3+m)\frac{\pi}{6}\right]}{3+m} + \frac{\sin\left[(3-m)\frac{\pi}{6}\right]}{3-m} \right], & \text{otherwise.} \end{cases} \quad (8.3)$$

Thus we solve (2.5a–c) for each Fourier mode numerically as described in § 4, substituting  $\exp[-(24\phi/\pi)^2/2]$  for  $Q^m$ , and then sum the solutions according to (8.2) and (8.3).

The results are presented in figure 19 for truncation order 50, i.e.  $m = -50, \dots, 50$ . The convergence of the Fourier series in (8.2) to the forcing (8.1) is shown in figure 13 of the supplementary material. With the chosen truncation order 50, the two are nearly indistinguishable, whereas for truncation order 25, there are still noticeable differences. As noted by Bretherton & Sobel (2003), if the damping term in the continuity equation is zero, then the Matsuno–Gill model does not admit a non-zero zonal mean. Thus to avoid



complications when the damping term in the continuity equation is small, we remove the  $m = 0$  Fourier mode from the results in this figure. As in [figure 2](#), the leftmost column corresponds to the applied forcing, which is identical in all cases in this figure. Unlike [figure 2](#) (and all other previous figures), the longitudinal domain corresponds to  $[-\pi, \pi]$  (not one zonal period). The meridional domain still extends from the south pole to the north pole.

In the response to moderate damping and fast rotation ([figure 19b](#)), we identify Gill’s version of the fleur-de-lis in the geopotential height field (red square). In the response to light damping and fast rotation (first row), we identify the Sverdrup balance approximation shown in Bretherton & Sobel (2003) for the Matsuno–Gill model on the equatorial  $\beta$ -plane in the limit of no damping (also discussed in Neelin 1988).

The key observation from [figure 19](#) relates to the far-field response. In the response to light damping and moderate rotation ([figure 19d](#)), we identify the WTG approximation obtained in Bretherton & Sobel (2003) for the Matsuno–Gill model on the equatorial  $\beta$ -plane. While the solutions in this case resemble those of Bretherton & Sobel (2003), they correspond to different regimes in terms of the Rossby deformation radius. In Bretherton & Sobel (2003), the e-folding of the forcing is  $\sqrt{2}R_{eq}$ , where  $R_{eq}$  is the equatorial Rossby deformation radius, and the resulting geopotential under the WTG approximation decays over several  $R_{eq}$ . The equatorial Rossby radius of deformation in the scaling of the present work is  $R_{eq} = (gHa^2/4\Omega^2)^{1/4} = a\epsilon^{-1/4}$ . For moderate rotation, where  $\epsilon^{1/2} = 1$ ,  $R_{eq} = a = 6371$  km, or approximately  $57^\circ$  latitude. Thus, in contrast to the WTG on the equatorial  $\beta$ -plane, the e-folding of the forcing in (8.1) corresponds to approximately  $0.13R_{eq}$ , and the geopotential decays within one  $R_{eq}$ . Considering the wave spectra in [table 2](#), we see that the cases exhibiting far-field response are also the ones whose response is dominated by the Rossby waves (except for the moderate damping and moderate rotation case).

The results of this section demonstrate the generality and applicability of the results of the previous sections to the case of localized forcing. This is particularly important for applications such as quasi-stationary Rossby waves forced by the Madden–Julian oscillation (MJO) or El Niño, where the forcing is indeed localized.

## 9. Summary and discussion

In its essence, the Matsuno–Gill model is a driven harmonic oscillator in the atmosphere and oceans. An external force (a heat source or topography) provides potential energy, some of which is transferred to kinetic energy, some dissipated by a linear drag, and the long-term response consists solely of those eigenmodes (equatorial waves) that are closest to being in resonance with the forcing. It is this essence that makes the Matsuno–Gill model instrumental in the study of the atmosphere and oceans. Yet in its original formulation, the model employs the  $\beta$ -plane approximation, which, depending on the celestial body in question and the external forcing, may limit its applicability to the equatorial region. In the present work, we have extended the Matsuno–Gill model to the sphere.

The key difference between the model on the  $\beta$ -plane and its counterpart on the sphere lies in their parameter spaces. When applied to the equator, the  $\beta$ -plane approximation greatly simplifies the analysis by coupling the planetary rate of rotation and mean radius, thereby reducing the parameter space. In fact, on the equatorial  $\beta$ -plane, the Matsuno–Gill model can be reduced to a one-dimensional parameter space, consisting solely of the non-dimensional rate of damping ( $\gamma$ ), whereas on the sphere, it can be reduced only to

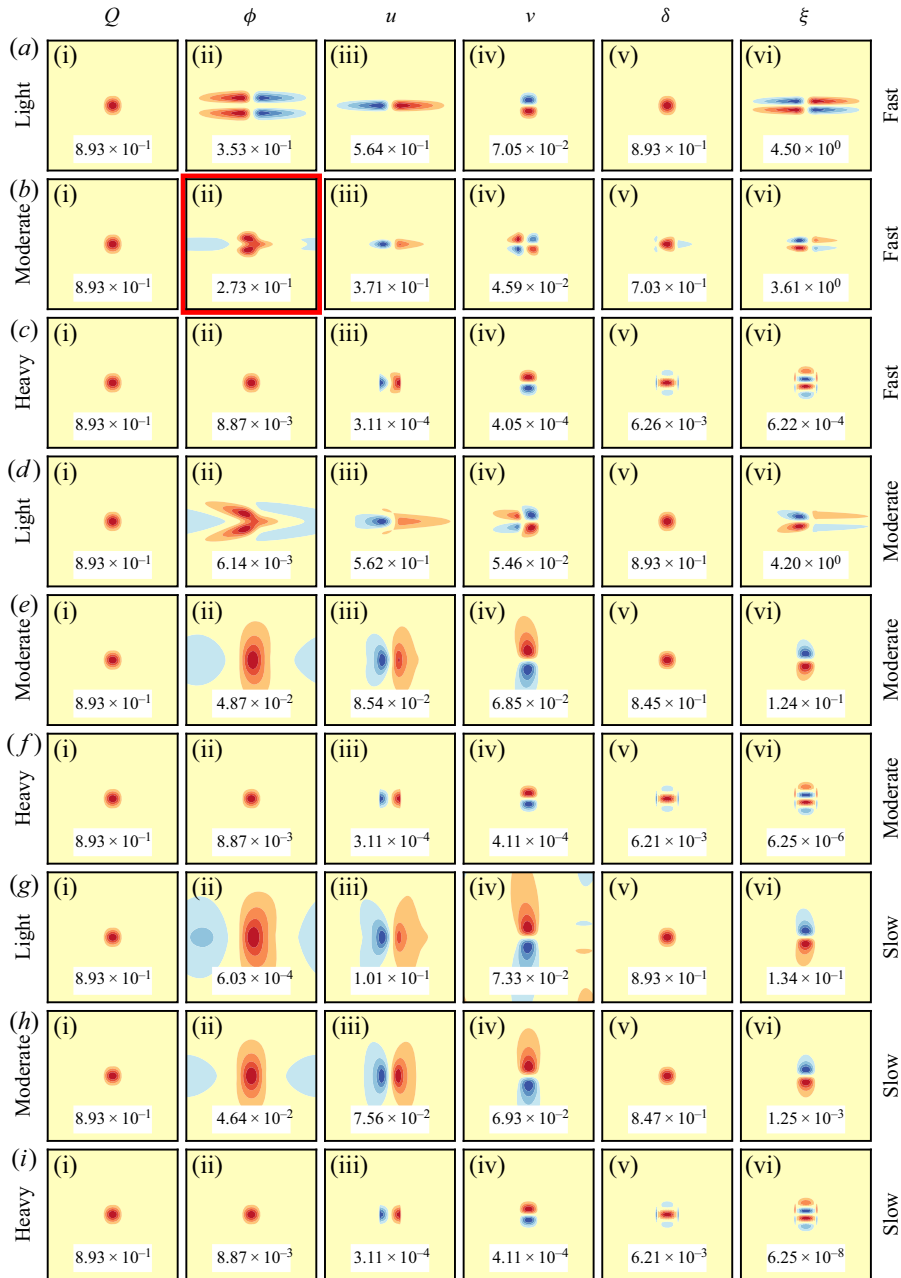


Figure 19. Steady-state response to the local forcing in (8.1). In order from (i) to (vi): the prescribed forcing, geopotential height, zonal wind, meridional wind, divergence and vorticity. The rows correspond to the different samples of the  $(\gamma, \epsilon^{1/2})$  plane summarized in table 1. The damping and rotation rates for each case (row) are labelled on the left and right edges, respectively. The meridional domain in each panel extends from the south pole to the north pole. The longitudinal domain corresponds  $[-\pi, \pi]$ . Contours range from  $-1$  (deep blue) to  $1$  (strong red) every  $0.2$ , excluding  $0$ . For the sake of presentation, each panel is normalized on its global absolute maximum, given in white text boxes.

a two-dimensional parameter space  $(\gamma, \epsilon^{1/2})$ . Depending on the choice of scaling, the additional parameter may play the role of the non-dimensional rate of rotation (the present choice), the non-dimensional gravitational acceleration or the non-dimensional speed of gravity waves. Regardless of its interpretation, its effect is to alter the eigenmodes of the free system (the ‘natural frequencies’ of the harmonic oscillator). Thus, unlike the solutions obtained by Matsuno (1966) and Gill (1980), where the long-term response to a symmetric forcing consists solely of Kelvin and Rossby waves, the response of the Matsuno–Gill model on the sphere consists of other waves as well, depending on  $\gamma$  and  $\epsilon^{1/2}$ .

By considering the different combinations of damping and rotation, relative to the time scale in which a gravity wave can propagate appreciably around the sphere, we are able to effectively span the  $(\gamma, \epsilon^{1/2})$  plane. We find that the  $\beta$ -plane approximation is accurate only with fast rotation,  $\epsilon^{1/2} \gg 1$ , while the particular solution studied by Matsuno (1966) and Gill (1980) is accurate only in the case of moderate damping (i.e. waves are damped on the same time scale as they propagate). The remaining regions of the parameter space can be described by appropriately simplified approximations.

With moderate rotation,  $\epsilon^{1/2} \approx 1$ , the most appropriate approximation depends on the damping. With light damping,  $\gamma \ll 1$ , the weak temperature gradient approximation (WTG), where the forcing is balanced by the flow divergence, is the most accurate. Less accurate, but analytic, solutions can be obtained with the geostrophic approximation, where the Coriolis and pressure gradient forces are also in balance. With heavy damping,  $\gamma \gg 1$ , accurate solutions can be found with a radiative relaxation approximation, where the forcing is balanced by the thermal dissipation.

With slow rotation,  $\epsilon^{1/2} \ll 1$ , and light damping,  $\gamma \ll 1$ , the WTG approximation is, again, the most accurate. With stronger damping,  $\gamma \approx 1$  or  $\gamma \gg 1$ , the solutions can be captured with the non-rotating approximation, where the Coriolis force is neglected. Finally, cases with moderate rotation and damping,  $\epsilon^{1/2} \approx \gamma \approx 1$ , are the most difficult, and do not fall into any limit. To some extent, however, they may be captured with the WTG approximation. Interestingly, the results of the present work suggest that in the context of the Matsuno–Gill model, the WTG approximation is more accurate on a global scale.

In terms of application to real geophysical fluids, we estimate that the majority of the Earth’s oceans fall within the region of the  $(\gamma, \epsilon^{1/2})$  plane corresponding to moderate damping and fast rotation, where the particular solutions obtained by Matsuno and Gill are applicable. Earth’s troposphere falls between the regions of light-to-moderate damping and fast-to-moderate rotation, half of which can be described by the  $\beta$ -plane approximation (fast rotation), and the other half by the WTG approximation (for sufficiently high forcing wavenumber). Earth’s stratosphere falls roughly between the regions of light-to-moderate damping and moderate rotation, which can be described by either the WTG approximation or the geostrophic approximation, but not the  $\beta$ -plane approximation. Likewise for Titan’s troposphere, which falls near the region of light damping and moderate rotation. Finally, Venus’ troposphere falls close to the moderate damping and moderate rotation region, where no approximation is satisfactory.

One caveat of the Matsuno–Gill model is the linearization. Both the present work and the original studies by Matsuno (1966) and Gill (1980) employ the linearized rotating shallow-water equations (RSWEs). However, the assumptions that justify the linearization involve both the amplitude and spatial distribution of the forcing. For highly oscillatory forcing, even small-amplitude perturbations can drive localized, non-negligible advection of momentum and/or mass. Moreover, the linearization is about a resting basic state with no mean flow. The results derived above will likely be altered significantly by the addition

of a mean flow, as such westerly flows enable Rossby wave propagation in the mid-latitudes (Hoskins & Karoly 1981) and act as a waveguide (Hoskins & Ambrizzi 1993). In particular, we expect a spherical model linearized about a basic state with non-zero zonal flow to exhibit a canonical poleward arching Rossby wavetrain. This wavetrain will reach latitudes in which the equatorial  $\beta$ -plane assumption is grossly violated, necessitating the spherical formulation.

In formulating the Matsuno–Gill model, we have conceptualized the prescribed forcing as being due to time-independent external forces, e.g. topography or solar radiation. One can also consider the quasi-steady-state response to internal variability on larger time scales, e.g. the quasi-stationary Rossby wave response to convective forcing by the MJO or El Niño. The Matsuno–Gill model turns out to be a useful theoretical framework for understanding the subsequent responses even for such quasi-stationary heat sources (Adames & Wallace 2014; Zhang *et al.* 2020). Specifically, the subtropical highs forced by the El Niño–Southern Oscillation (ENSO) and the MJO can be accounted for, albeit in a conceptual sense, by the Matsuno–Gill model. These subtropical highs, and more generally the entirety of the spherical solutions considered here, particularly those in § 8, will change if a mean flow is added (Monteiro *et al.* 2014). Future work should consider coupling the solutions of the present work with a mean flow to better understand the remote response to the tropical convective forcing associated with the MJO and El Niño. The classical papers on how the mid-latitude lows come about (e.g. Hoskins & Karoly 1981) assume or impose a given subtropical convergence anomaly as a starting point. To date, there is no single overarching theory that can account for both the near-field (i.e. within the tropics) and far-field (i.e. mid-latitude) responses to the MJO or El Niño. Solutions of the Matsuno–Gill problem on the sphere linearized about an appropriate background wind, however, may be able to account for the entirety of the Rossby wavetrain forced from the tropics.

Another caveat of the Matsuno–Gill model is the source of the linear damping. The physical justification for the use of linear damping in the atmosphere has been examined by several authors throughout the years. By analysing the steady-state vorticity budget, Holton & Colton (1972) found it necessary to have ostensibly heavy damping in order to obtain comparable results to the observed 200 hPa vorticity field during June–August 1967. They conjectured that the required heavy damping effectively plays the role of upward eddy momentum flux associated with subgrid-scale convection. By comparing the same observational data with general circulation model simulations, Sardeshmukh & Held (1984) suggested that the required heavy damping can also be explained by the resolved advection. Lin, Mapes & Han (2008) further examined the contributions of these two mechanisms to the effective linear damping in the context of the Walker circulation. By examining the linearized zonal momentum budget in reanalysis data, they found that the two mechanisms have different contributions in different regions of the circulation. Finally, Romps (2014) found that convective momentum transport can explain the heavy damping of the large-scale circulation depending on the vertical wavenumbers. Regardless of the particular mechanism, these authors agree that heavy linear damping acts as a surrogate for missing nonlinearities. In the spirit of the present work, one may conclude that when it comes to the fleur-de-lis, ‘vive la résistance’.

An additional caveat relating to the linear damping in the Matsuno–Gill model, not considered by the above authors, is the use of identical rates of ‘mechanical’ damping in the momentum equations and ‘thermal’ damping in the continuity equation. The former can only remove energy, whereas the latter plays the role of both dissipation and relaxation and thus can also add energy. As a result, the rate of energy intake in the Matsuno–Gill

model is identical to the rate of energy loss, which is an unlikely scenario, especially if the linear damping is to be considered as a surrogate for the missing nonlinearities. Future work should consider the Matsuno–Gill model in the presence of different mechanical and thermal damping rates (ideally, the continuity equation should include separate damping and relaxation terms), and the observational justification for doing so.

In some sense, the approach employed by Matsuno and Gill follows the ‘maximum simplification’ approach of Lorenz (1960, 1963), where the problem is discretized using the most drastic truncation that yields sensible dynamics. Matsuno and Gill use only the lowest wave modes in the forcing, namely the Kelvin and MRG waves. However, since they use only the geopotential associated with these modes, the forcing projects on other modes as well.

These caveats said, we have shown that extending the Matsuno–Gill model from the  $\beta$ -plane to the sphere opens up a much richer space of solutions and applications. Not only does it allow us to capture solutions that extend sufficiently poleward for spherical geometry to play a role, but the addition of a second parameter to capture the relative effects of rotation and damping allows one to explore additional regimes outside the scope of the original model. As we have shown, the original model is appropriate only when the rotation is fast relative to the time scale in which waves can appreciably propagate about the sphere. This is the most appropriate regime for Earth’s oceans, and to a lesser extent the tropical troposphere – Matsuno and Gill knew what they were doing – but other regimes, both on Earth (e.g. our stratosphere) and beyond (e.g. Venus and Titan) become accessible with a formulation on the sphere.

**Supplementary material.** Supplementary material is available at <https://doi.org/10.1017/jfm.2023.369>.

**Acknowledgements.** The authors thank Dr O. Adam from the Hebrew University of Jerusalem for helpful discussion on tropical dynamics.

**Funding.** O.S. and E.P.G. acknowledge support from Schmidt Futures, a philanthropic initiative founded by Eric and Wendy Schmidt, as part of the Virtual Earth System Research Institute (VESRI). E.P.G. acknowledges further support from the National Science Foundation (NSF, grant OAC-2004572). C.I.G. is supported by the ISF-NSFC joint research programme (ISF grant 3259/19) and by ISF grant 1727/21. C.I.G. and E.P.G. are supported by the US–Israel Binational Science Foundation (BSF) grant 2020316.

**Declaration of interests.** The authors report no conflict of interest.

#### Author ORCIDs.

-  Ofer Shamir <https://orcid.org/0000-0003-3079-5812>;
-  Chaim I. Garfinkel <https://orcid.org/0000-0001-7258-666X>;
-  Edwin P. Gerber <https://orcid.org/0000-0002-6010-6638>;
-  Nathan Paldor <https://orcid.org/0000-0002-4419-4201>.

#### REFERENCES

- ADAM, O. 2018 Zonally varying ITCZs in a Matsuno–Gill-type model with an idealized Bjerknes feedback. *J. Adv. Model. Earth Syst.* **10** (6), 1304–1318.
- ADAMES, Á.F. & KIM, D. 2016 The MJO as a dispersive, convectively coupled moisture wave: theory and observations. *J. Atmos. Sci.* **73** (3), 913–941.
- ADAMES, Á.F. & WALLACE, J.M. 2014 Three-dimensional structure and evolution of the vertical velocity and divergence fields in the MJO. *J. Atmos. Sci.* **71** (12), 4661–4681.
- ARNOLD, N.P., TZIPERMAN, E. & FARRELL, B. 2012 Abrupt transition to strong superrotation driven by equatorial wave resonance in an idealized GCM. *J. Atmos. Sci.* **69** (2), 626–640.
- BELTON, M.J.S., SMITH, G.R., SCHUBERT, G. & DEL GENIO, A.D. 1976 Cloud patterns, waves and convection in the Venus atmosphere. *J. Atmos. Sci.* **33** (8), 1394–1417.



- BIELLO, J.A. & MAJDA, A.J. 2005 A new multiscale model for the Madden–Julian oscillation. *J. Atmos. Sci.* **62** (6), 1694–1721.
- BOYD, J.P. 1985 Barotropic equatorial waves: the nonuniformity of the equatorial beta-plane. *J. Atmos. Sci.* **42** (18), 1965–1967.
- BOYD, J.P. 2018 *Dynamics of the Equatorial Ocean*. Springer.
- BOYD, J.P. & ZHOU, C. 2008 Uniform asymptotics for the linear Kelvin wave in spherical geometry. *J. Atmos. Sci.* **65** (2), 655–660.
- BRETHERTON, C.S. & SOBEL, A.H. 2003 The Gill model and the weak temperature gradient approximation. *J. Atmos. Sci.* **60** (2), 451–460.
- CHAO, W.C. 1987 On the origin of the tropical intraseasonal oscillation. *J. Atmos. Sci.* **44** (15), 1940–1949.
- CHELTON, D.B., DESZOEKE, R.A., SCHLAX, M.G., EL NAGGAR, K. & SIWERTZ, N. 1998 Geographical variability of the first baroclinic Rossby radius of deformation. *J. Phys. Oceanogr.* **28** (3), 433–460.
- COVEY, C. & SCHUBERT, G. 1982 Planetary-scale waves in the Venus atmosphere. *J. Atmos. Sci.* **39** (11), 2397–2413.
- DALLASANTA, K., GERBER, E.P. & TOOHEY, M. 2019 The circulation response to volcanic eruptions: the key roles of stratospheric warming and eddy interactions. *J. Clim.* **32** (4), 1101–1120.
- DE-LEON, Y. & PALDOR, N. 2011 Zonally propagating wave solutions of Laplace tidal equations in a baroclinic ocean of an aqua-planet. *Tellus A* **63** (2), 348–353.
- DE-LEON, Y., PALDOR, N. & GARFINKEL, C.I. 2020 Barotropic modes, baroclinic modes and equivalent depths in the atmosphere. *Q. J. R. Meteorol. Soc.* **146** (730), 2096–2115.
- DEL GENIO, A.D. & ROSSOW, W.B. 1990 Planetary-scale waves and the cyclic nature of cloud top dynamics on Venus. *J. Atmos. Sci.* **47** (3), 293–318.
- FRITTS, D.C. & ALEXANDER, J.M. 2003 Gravity wave dynamics and effects in the middle atmosphere. *Rev. Geophys.* **41** (1).
- GARFINKEL, I.C., FOUXON, I., SHAMIR, O. & PALDOR, N. 2017 Classification of eastward propagating waves on the spherical Earth. *Q. J. R. Meteorol. Soc.* **143** (704), 1554–1564.
- GARFINKEL, C.I., SHAMIR, O., FOUXON, I. & PALDOR, N. 2021 Tropical background and wave spectra: contribution of wave–wave interactions in a moderately nonlinear turbulent flow. *J. Atmos. Sci.* **78** (6), 1773–1789.
- GILL, A.E. 1980 Some simple solutions for heat-induced tropical circulation. *Q. J. R. Meteorol. Soc.* **106** (449), 447–462.
- HOLTON, J.R. & COLTON, D.E. 1972 A diagnostic study of the vorticity balance at 200 mb in the tropics during the northern summer. *J. Atmos. Sci.* **29** (6), 1124–1128.
- HOSKINS, B.J. & AMBRIZZI, T. 1993 Rossby wave propagation on a realistic longitudinally varying flow. *J. Atmos. Sci.* **50** (12), 1661–1671.
- HOSKINS, B.J. & KAROLY, D.J. 1981 The steady linear response of a spherical atmosphere to thermal and orographic forcing. *J. Atmos. Sci.* **38** (6), 1179–1196.
- HOUGH, S.S. 1897 On the application of harmonic analysis to the dynamical theory of the tides. Part I. On Laplace’s ‘oscillations of the first species’ and on the dynamics of ocean currents. *Phil. Trans. R. Soc. Lond. A* **189**, 201–257.
- HOUGH, S.S. 1898 On the application of harmonic analysis to the dynamical theory of the tides. Part II. On the general integration of Laplace’s dynamical equations. *Phil. Trans. R. Soc. Lond. A* **191**, 139–185.
- KACIMI, A. & KHOUIDER, B. 2018 The transient response to an equatorial heat source and its convergence to steady state: implications for MJO theory. *Clim. Dyn.* **50** (9–10), 3315–3330.
- LIN, J.L., MAPES, B.E. & HAN, W. 2008 What are the sources of mechanical damping in Matsuno–Gill-type models? *J. Clim.* **21** (2), 165–179.
- LONGUET-HIGGINS, M.S. 1968 The eigenfunctions of Laplace’s tidal equation over a sphere. *Phil. Trans. R. Soc. Lond. A* **262** (1132), 511–607.
- LORENZ, E.N. 1960 Maximum simplification of the dynamic equations. *Tellus* **12** (3), 243–254.
- LORENZ, E.N. 1963 Deterministic nonperiodic flow. *J. Atmos. Sci.* **20** (2), 130–141.
- LUTSKO, N.J. 2018 The response of an idealized atmosphere to localized tropical heating: superrotation and the breakdown of linear theory. *J. Atmos. Sci.* **75** (1), 3–20.
- MAJDA, A.J. & STECHMANN, S.N. 2009 The skeleton of tropical intraseasonal oscillations. *Proc. Natl Acad. Sci.* **106** (21), 8417–8422.
- MATSUNO, T. 1966 Quasi-geostrophic motions in the equatorial area. *J. Meteorol. Soc. Japan* **44** (1), 25–43.
- MITCHELL, J.L., ÁDÁMKOVICS, M., CABALLERO, R. & TURTLE, E.P. 2011 Locally enhanced precipitation organized by planetary-scale waves on Titan. *Nat. Geosci.* **4** (9), 589–592.
- MONTEIRO, J.M., ADAMES, Á.F., WALLACE, J.M. & SUKHATME, J.S. 2014 Interpreting the upper level structure of the Madden–Julian oscillation. *Geophys. Res. Lett.* **41** (24), 9158–9165.



## Matsuno–Gill model on the sphere

- MÜLLER-WODARG, I., GRIFFITH, C.A., LELLOUCH, E. & CRAVENS, T.E. 2014 *Titan: Interior, Surface, Atmosphere, and Space Environment*, vol. 14. Cambridge University Press.
- NEELIN, D.J. 1988 A simple model for surface stress and low-level flow in the tropical atmosphere driven by prescribed heating. *Q. J. R. Meteorol. Soc.* **114** (481), 747–770.
- PALDOR, N., DE-LEON, Y. & SHAMIR, O. 2013 Planetary (Rossby) waves and inertia–gravity (Poincaré) waves in a barotropic ocean over a sphere. *J. Fluid Mech.* **726**, 123–136.
- PALDOR, N., FOUXON, I., SHAMIR, O. & GARFINKEL, C.I. 2018 The mixed Rossby–gravity wave on the spherical Earth. *Q. J. R. Meteorol. Soc.* **144** (715), 1820–1830.
- PERALTA, J., *et al.* 2020 A long-lived sharp disruption on the lower clouds of Venus. *Geophys. Res. Lett.* **47** (11), e2020GL087221.
- ROMPS, D.M. 2014 Rayleigh damping in the free troposphere. *J. Atmos. Sci.* **71** (2), 553–565.
- SARDESHMUKH, P.D. & HELD, I.M. 1984 The vorticity balance in the tropical upper troposphere of a general circulation model. *J. Atmos. Sci.* **41** (5), 768–778.
- SHAMIR, O., GARFINKEL, C.I., ADAM, O. & PALDOR, N. 2021a A note on the power distribution between symmetric and antisymmetric components of the tropical brightness temperature spectrum in the wavenumber–frequency plane. *J. Atmos. Sci.* **78** (11), 3473–3476.
- SHAMIR, O., SCHWARTZ, C., GARFINKEL, C.I. & PALDOR, N. 2021b The power distribution between symmetric and antisymmetric components of the tropical wavenumber–frequency spectrum. *J. Atmos. Sci.* **78** (6), 1983–1998.
- SHOWMAN, A.P. & POLVANI, L.M. 2010 The Matsuno–Gill model and equatorial superrotation. *Geophys. Res. Lett.* **37** (18).
- SMITH, M.D., GIERASCH, P.J. & SCHINDER, P.J. 1992 A global traveling wave on Venus. *Science* **256** (5057), 652–655.
- SOBEL, A. & MALONEY, E. 2012 An idealized semi-empirical framework for modeling the Madden–Julian oscillation. *J. Atmos. Sci.* **69** (5), 1691–1705.
- SVEDHEM, H., TITOV, D.V., TAYLOR, F.W. & WITASSE, O. 2007 Venus as a more Earth-like planet. *Nature* **450** (7170), 629–632.
- TOOHEY, M., KRÜGER, K., BITTNER, M., TIMMRECK, C. & SCHMIDT, H. 2014 The impact of volcanic aerosol on the northern hemisphere stratospheric polar vortex: mechanisms and sensitivity to forcing structure. *Atmos. Chem. Phys.* **14** (23), 13063–13079.
- TREFETHEN, L.N. 2000 *Spectral Methods in MATLAB*, vol. 10. SIAM.
- WILKA, C., SOLOMON, S., CRONIN, T.W., KINNISON, D. & GARCIA, R. 2021 Atmospheric chemistry signatures of an equatorially symmetric Matsuno–Gill circulation pattern. *J. Atmos. Sci.* **78** (1), 107–116.
- YAMAMOTO, M. 2019 Equatorial Kelvin-like waves on slowly rotating and/or small-sized spheres: application to Venus and Titan. *Icarus* **322**, 103–113.
- ZHANG, C., ADAMES, Á.F., KHOUIDER, B., WANG, B. & YANG, D. 2020 Four theories of the Madden–Julian oscillation. *Rev. Geophys.* **58** (3), e2019RG000685.
- ZHU, J., LIU, Y., XIE, R. & CHANG, H. 2018 A comparative analysis of the impacts of two types of El Niño on the central and eastern Pacific ITCZ. *Atmosphere* **9** (7), 266.